



U.O.C

# Velocity Map Imaging of Rb

DIAMANTOPOULOU NIKI

Στην Αφροδίτη και τον Βασίλη

## Ευχαριστίες

Σε αυτό το σημείο θα ήθελα να ευχαριστήσω τη μητέρα μου που ήταν πάντα εκεί . Χωρίς αυτήν τίποτα δεν θα ήταν εφικτό. Την ευχαριστώ για όλα.

Θα ήθελα να ευχαριστήσω τον πατέρα μου που πάντα με στήριζε και με στηρίζει.

Επίσης τον καθηγητή μου Θεοφάνη Κιτσόπουλο που μου έδωσε την ευκαιρία να δουλέψω μαζί του και να μάθω σημαντικά πράγματα.

Τον Δημήτριο Άγγλο που σε όλη αυτήν την προσπάθεια με έχει στηρίξει και βοηθήσει πάρα πολύ.

Τον Σταύρο Φαράντο που μέ έκανε να αγαπήσω τη φυσικοχημεία .

Τον καθηγητή Dave Parker όπου μέρος αυτής της εργασίας έλαβε χώρα στο εργαστήριό του.

Τον Andre Eppink για την ουσιαστική βοήθεια του σε αυτή τη δουλειά, για τις αμέτρητες συζητήσεις μας που με βοήθησαν να βρώ το σωστό δρόμο και να ανταπεξέλθω στις απαιτήσεις του πειράματος, για την υποστηρίξη του και τέλος στο γεγονός ότι πίστεψε σε μένα και μου έδωσε μια μοναδική ευκαιρία . Πάντα θα προσπαθώ να μην τον απογοητεύσω. Σε ευχαριστώ andre.....

Τον Πέτρο Σαμαρτζή, τον φίλο και συνεργάτη που με τις “άπειρες “ γνώσεις του πάντα μας βάζει στο σωστό δρόμο. Δεν υπάρχουν λόγια για τον πέτρο πιστεύω.. Χωρίς αυτόν είμαστε χαμένοι..

Τον Νίκο Στρατηγάκη που πάντα πιστεύει σε μένα , είναι πάντα εκεί και πάντα με υποστηρίζει. Τον ευχαριστώ πολύ καθώς μου έμαθε πολλά χρήσιμα πράγματα για τη φυσικοχημεία.. Τον ευχαριστώ για τις ευχάριστες συζητήσεις.



# Coherent Control in Rubidium probed with Velocity Map Imaging

Coherent Control in Rb probed with VMI

Niki V. Diamantopoulou

Master thesis , University of Crete, UOC, Department of Chemistry

Institute of Electronic Structure and Laser(IESL)

Foundation of Research and Technology - Hellas (FORTH)

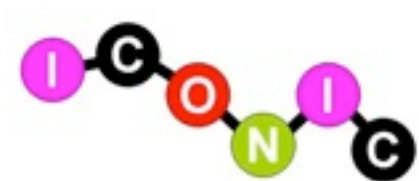
University of Nijmegen -Institute of Molecular Physics

Supervisors : PROF. DR. THEOFANIS N. KITSOPOULOS

PROF. DR. D.H. PARKER

DR. ANDRE EPPINK

PROF. DR. W.J. VAN DER ZANDE



This research is part of ICONIC research program

[www.ru.nl/iconic](http://www.ru.nl/iconic)

## Περίληψη

Στην παρούσα εργασία παρουσιάζεται ένας τρόπος ελέγχου της κατανομής των ηλεκτρονίων στην πρώτη διεγερμένη κατάσταση του Ρουβιδίου.

Χρησιμοποιώντας την τεχνική τροποποίησης παλμών μέσω αλλαγής της πόλωσης ενός παλμού της τάξης των φεμπτοδευτερολέπτων παρουσιάζεται ένας αποτελεσματικός τρόπος να ελεγχθεί η μεταφορά στροφορμής στην πρώτη διεγερμένη κατάσταση του Ρουβιδίου. Αυτό επιτεύχθηκε μετρώντας την ικανότητα διέγερσης στα επιμέρους μαγνητικά υποεπίπεδα της πρώτης διεγερμένης κατάστασης τού Ρουβιδίου.

Οι μετρήσεις που πάρθηκαν αποτελούν παρατήρηση της εξέλιξης της κυματοσυνάρτησης σε πραγματικό χρόνο, που οφείλεται στην αλλαγή της στροφορμής, και για αυτό χρησιμοποιήθηκε η τεχνική της χαρτογράφησης ταχυτήτων.

Κάνοντας περαιτέρω ανάλυση πλυθισμού στα επιμέρους μαγνητικά υποεπίπεδα της πρώτης διεγερμένης κατάστασης ανακαλύψαμε έναν καινούριο τρόπο ελέγχου της μεταφοράς στροφορμής.

Ανακαλύψαμε πώς οι φασματικές ιδιότητες τού παλμού διέγερσης παίζουν σημαντικό ρόλο στην μεταφορά στροφορμής στην πρώτη διεγερμένη κατάσταση τού ρουβιδίου.

Όταν βρίσκομαι σε διέγερση σε συντονισμό στην πρώτη διεγερμένη κατάσταση η δυναμική στροφορμής δεν μπορεί να εξηγηθεί απόλυτα από τις φασματικές ιδιότητες τού παλμού διέγερσης παρ'όλα αυτά θα πρέπει να λαμβάνονται υπ'όψιν.

Όταν βρισκόμαστε σε διέγερση σε μη-συντονισμό στην πρώτη διεγε-

ρμένη κατάσταση η δυναμική στροφορμής περιγράφεται πλήρως από τις φασματικές ιδιότητες τού παλμού διέγερσης και μπορεί να προβλεφθεί από αυτές.

Τα αποτελέσματα μας δίνουν μια νέα διάσταση για τον έλεγχο αντιδράσεων, για οπτικό προσανατολισμό αλλά και για προσανατολισμό τού σπίν.

Επιπλέον καταφέραμε να δείξουμε πώς με ένα τέτοιου είδους πείραμα μπορούμε να ελέγξουμε εν - μέρει την κατανομή τών ηλεκτρονίων και πιο συγκεκριμένα να δούμε πώς αλλάζουν τα τροχιακά σε πραγματικό χρόνο.

# Contents

- 1 General Concepts
  - 1.1 Introduction to Molecular Dynamics
  - 1.2 Ion and Velocity Map Imaging
  - 1.3 Coherent Control

- 2 Experimental set-up
  - 2.1 Velocity map Imaging apparatus
  - 2.2 Femtosecond lasers
  - 2.3 pulse shaper

- 3 Spectroscopy
  - 3.1 Spectroscopy of Rb

- 4 Results and discussion

Conclusion

References

## **Abstract**

In this thesis, coherent control of one-photon excitation in Rb using ultrashort laser pulses is discussed. By using polarization-shaping of a hundred femtosecond laser pulse it is possible to control the magnitude of angular momentum in excited state in rubidium. This is achieved by controlling excitation efficiencies to individual magnetic sub-levels of excited state in rubidium. It is shown, that angular momentum in excited state can be controlled by zero-angular momentum laser pulses, containing only linearly polarized spectral components. During a resonant two-photon excitation a net angular momentum can be transferred to rubidium atoms. However, even during a one-photon excitation angular momentum in excited state is changing in a nonintuitive way, and transiently can be controlled. In this thesis results of coherent control of the transient angular momentum during a resonant one-photon excitation are discussed. The experimental study was done using pump-probe technique and velocity map imaging. The rubidium was excited by a shaped laser pulse and ionized by a probe pulse. Using VMI technique the velocity distribution of the photoelectrons was measured to characterize the angular momentum in excited state in rubidium. In this thesis we present results on real-time observation of the changes of the wave-function induced by the angular momentum change during the one-photon excitation.

# Chapter 1

## General Concepts

### Velocity map imaging in molecular dynamics

#### Abstract

In this chapter we present the concepts on which the experimental work and discussion of the following chapters is based. Following a brief introduction to Molecular Dynamics, we discuss the velocity map imaging technique including the improved 2D ion imaging using electrostatic lenses and relevant applications. We also describe the principles of coherent control relevant to current work.

## **1.1 Molecular Dynamics**

Understanding how chemical reactions occur at the molecular level and how to control them is of fundamental importance to chemists and interdisciplinary areas such as materials science, nano-science, environmental science and astrochemistry. Molecular dynamics studies the mechanisms of chemical and physical transformations of matter at the molecular level.[1]

The first step in understanding chemistry is to consider that chemical reactions proceed through collisions. During a collision there can be exchange of momentum, energy and mass (atoms or groups of atoms). If only momentum changes, the collision is called “elastic”. If there is also exchange of energy, the collision is “inelastic”, while exchange of atoms falls into the field of reactive scattering.[2] Absorption of one or more photons increases the amount of the internal energy of the system and finally it can be released in the form of heat or radiation ( collisional or radiative decay) or can lead to chemical change (photodissociation or ionization).

These processes can be denoted symbolically as follows:



***inelastic collisions***



***reaction process***



***photodissociation***

Note that A B and C can be atoms or molecular fragments which can be in internally excited states. A bimolecular reaction can be considered as a full collision event: the reactants come together and form an intermediate complex (or transition state) after which newly formed products are formed which fly apart and photodissociation process can be considered as a half collision event: the fragments are also formed from an intermediate complex, but before photo-excitation the molecule was in a bound state.

Total cross sections ( $\sigma$ ) for a full collision are generally given as an excitation function  $\sigma(E_{\text{col}})$ , a function of collision energies ( $E_{\text{col}}$ ), while those for a half a collision are referred to as absorption cross section  $\sigma(\nu)$ , a function of photon energies  $h\nu$ , (or frequency  $\nu$ , wavelength  $\lambda$ ), as commonly used in spectroscopy. The total cross section, angular distribution and (TKER) total kinetic energy release are very important measurements for molecular dynamics.

The study of photodissociation processes is from experimental viewpoint quite appealing because is made of laser technology that is available at present. For example by using a pulsed laser the exact moment of excitation can be determined.

## **Newton's Spheres**

Let's consider a general process  $AB^* \rightarrow A + B + \text{TKER}$  where TKER (kinetic energy release) is the excess energy left over after partitioning of internal energy in the A and B products. Conservation of energy and momentum in the kinetic energy leads to partitioning of the kinetic energy of the fragments as follows:  $KE_A = (M_B / M_{AB})^* \text{KER}$  and  $KE_B = (M_A / M_{AB})^* \text{KER}$ . In this analysis the factor  $M_B / M_{AB}$  or  $(M_A / M_{AB})$  will be called the mass partitioning factor. For photoionization  $m_{e^-} \ll M_{m^+}$ , thus the photoelectron receives essentially all of the KER, while for photodissociation of a homo-nuclear diatomic reactant, the KER is equally shared between the two products.

Each photodissociation or photoionization process yields two partner fragments with equal momenta flying in opposite directions. The fragments are thus distributed in space on expanding spheres which are called Newton Spheres for the process[3]. They are called Newton Spheres because the fragments have to obey to Newton's laws of conservation of energy and momentum. By repeating the process thousands of times, a continuous view of the Newton Spheres emerges with a fixed radius and a characteristic intensity pattern on its surface.

In the next figure a simple 3-D Newton sphere is shown with polar coordinates  $r$  (not shown)  $\theta$  and  $\phi$ , where  $\theta$  is defined with respect to the  $z$ -axis (vertical axis in the figure),  $\phi$  is the azimuth angle and  $r$  the sphere radius. There is a fixed time period between formation and projection of the sphere, thus the sphere radius is directly proportional to velocity. Most of the surface intensity of this sphere is at the poles, representative of a typical  $\cos^2\theta$  distribution. Projection of the sphere onto a 2D surface will then form a filled circle with most of the intensity at the top and bottom outside edges of the circle.

newton sphere...

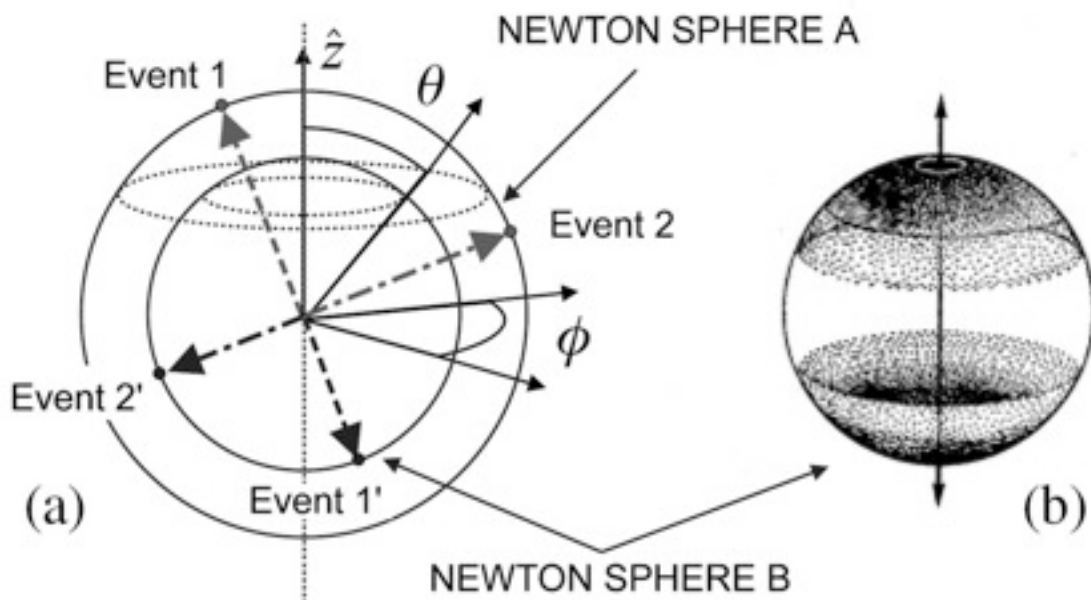


fig 1 : (a) a pair of newton spheres with spherical coordinates  $r$  (not shown),  $\theta$  and  $\phi$  where  $\theta$  is the polar angle with respect to the  $z$  axis ,  $\phi$  azimuthal angle and  $r$  sphere radius. Two events are shown in a with equal and opposite momentum (b) by summing up a large number of events(here for particle B) , a surface pattern emerges as shown. Most of the surface intensity of this examples is at the poles, representative of a  $\cos^2\theta$  distribution.

The distribution of a particle on a Newton's sphere is often anisotropic. In the case of photodissociation, there is often an anisotropic distribution of fragments with respect to the laser polarization direction( see next section) . In the case of imaging electrons emerging from a photoionization process, this distribution describes , the ejected electron waves which are coherent sums of the possible s, p, d, f ... wave-functions. (next section).

## **1.2 Ion and Velocity Map Imaging (VMI)**

Ion imaging techniques have proven to be of high value in the field of molecular reaction dynamics and are among the current state of the art techniques in the field. Imaging techniques provided the capability of probing full 3D particle distributions in a single image, which has the advantage of simultaneous detection of the kinetic energy release (KER) and the angular distribution of the particles (ions or electrons) of all velocities. The “traditional” ion imaging technique was widely applicable and compared well with the conventional time-of-flight (TOF) methods, however it lacked in resolution. The development of Velocity Map Imaging (VMI) of ions and electrons using electrostatic lenses, was a major improvement to 2D imaging and improved the resolution which really established imaging as a state of the art Molecular Dynamics technique.

In this section the technique of Velocity Map Imaging is outlined.[4] In the next picture the principle of the technique is illustrated.

In this section the technique of velocity map imaging is outlined.[4] In the next picture the principle of the technique is illustrated.

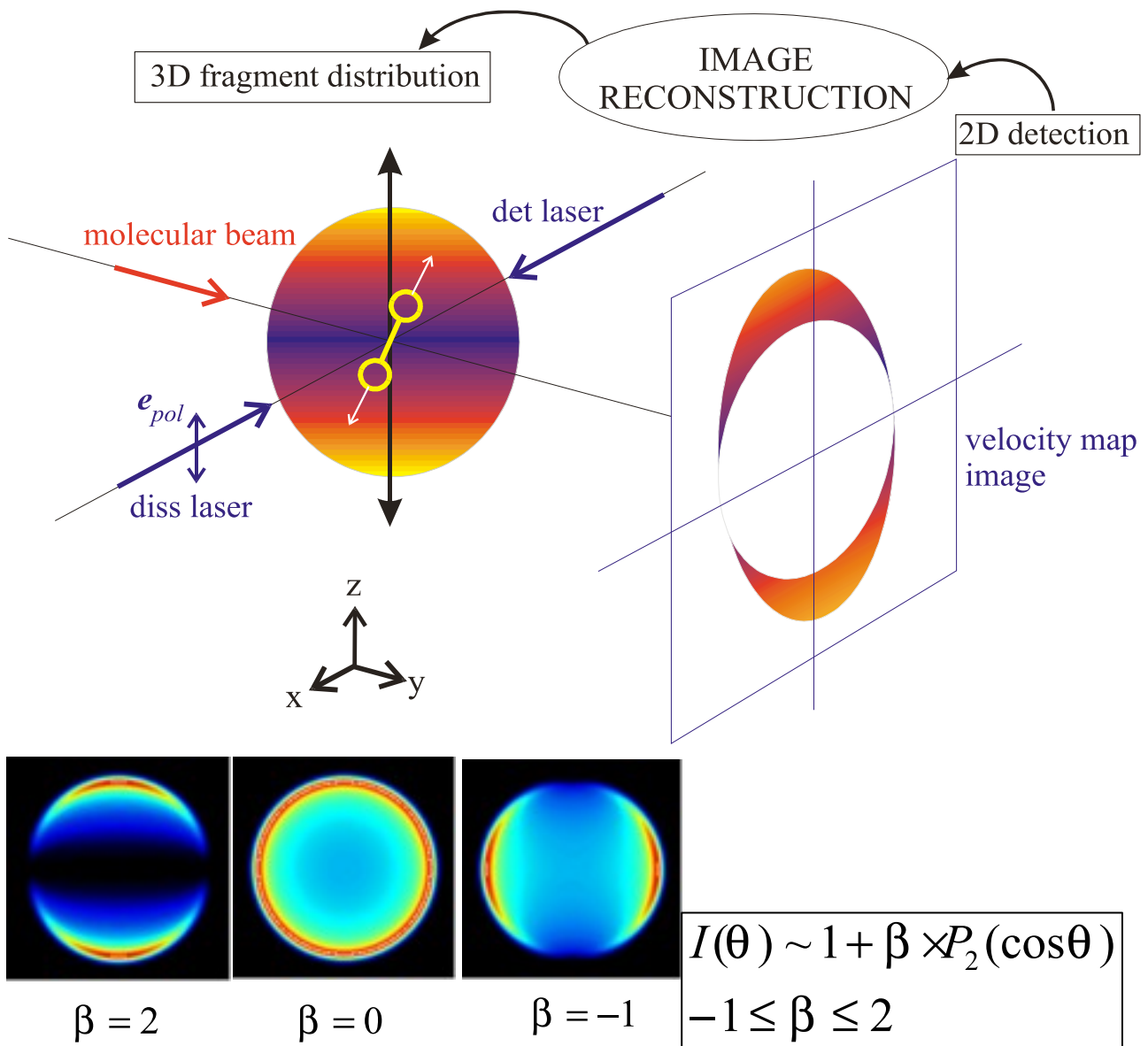


fig 2 ; the velocity map imaging technique is illustrated in this picture and angular distributions from images are obtained

The photodissociation or photoionization process takes place at the center of an electrostatic lens ( not shown) in this picture, where a molecular beam is crossed with a focused laser. The fragments are projected on expanding

spheres (cylindrically symmetric) around the polarization axis which move with the thermal velocity of the molecular beam. Using a second laser beam the fragments can be projected as ions using a REMPI (resonant enhanced multiphoton) ionization scheme).[5] The ions are flying in a time-of-flight (TOF) tube [6] and at the end they hit an imaging detector which consists of micro-channel plates (MCP's) [7] and phosphor screen. So this detector converts every ion into a spot on the phosphor screen. By recording the events on the phosphor screen using a CCD camera, images are obtained.

The image we obtain is a 2D projection of the initial 3D recoil velocity distribution of the selected fragment, thus we obtain crushed Newton spheres. By using the inverse Abel transform algorithm (or an equivalent reconstruction method) we can obtain the 3D distribution again.

A useful information that can be extracted from VMI technique is speed distribution. Considering this process  $AB + nh\nu \rightarrow (AB^*) \rightarrow A + B + TKER$ , molecule AB is excited upon absorption of one photon and fragments A and B are produced having total kinetic energy release (TKER). From conservation laws follows:  $T = T_A + T_B = nh\nu - D_0(AB) - E_{int}(A) - E_{int}(B)$ , where D is the dissociation energy and E is the internal energy of the fragments, n.hv is the photon energy. When neglecting thermal motion, conservation of momentum leads to

$m_A V_A + m_B V_B = 0$ , and this leads to simple speed and kinetic energy ratios  $\frac{U_A}{U_B} = \frac{m_B}{m_A} = \frac{T_B}{T_A}$ . TKER therefore is subdivided among the fragments

$T_A = \frac{m_B}{M} T, T_B = \frac{m_A}{M} T$ . Therefore, by studying the kinetic energy release or speed

distribution of just one fragment, TKER can be extracted  $T = \frac{1}{2} \mu U^2$ , where

$\mu = \frac{(m_A m_B)}{M}$ , the reduced mass and  $U = U_A + U_B$ , relative speed.

Another important information that can be extracted from the VMI technique is the angular distribution of the photo-fragments. Angular distributions can contain information of the photo-excitation as well as for the dynamical process. If a parent molecule is excited through an electric dipole transition, the transition dipole moment ( $\mu$ ) lies parallel to the electric vector e.. For instance for a parallel transition ( $\Sigma$ - $\Sigma$ ,  $\Pi$ - $\Pi$ ) the transition moment ( $\mu$ ) lies parallel to the

internuclear axis which leads to a preferential excitation of molecules with the internuclear axis aligned parallel to the laser polarization. If the recoil time of the fragment is short compared to the parent's molecule rotation time, (that means direct dissociation) thus parallel to the laser polarization ( $\cos^2 \theta$  distribution) .A transition  $\Sigma$ - $\Pi$  yields to a  $\sin^2 \theta$  distribution. If the transition has a mixture of parallel and perpendicular character, the angular distribution will be less anisotropic. The angular distribution is given from the equation shown in the figure above where  $\beta$  is the anisotropy parameter ,  $P_2$  is the second order Legendre polynomial and  $\theta$  is the angle.

In the figure above all the situations described in the paragraph above are shown. A parallel transition where  $\beta = 2$ , a perpendicular transition where  $\beta = -1$  and an isotropic distribution in space where  $\beta = 0$  .

### **VMI Experimental Set-up**

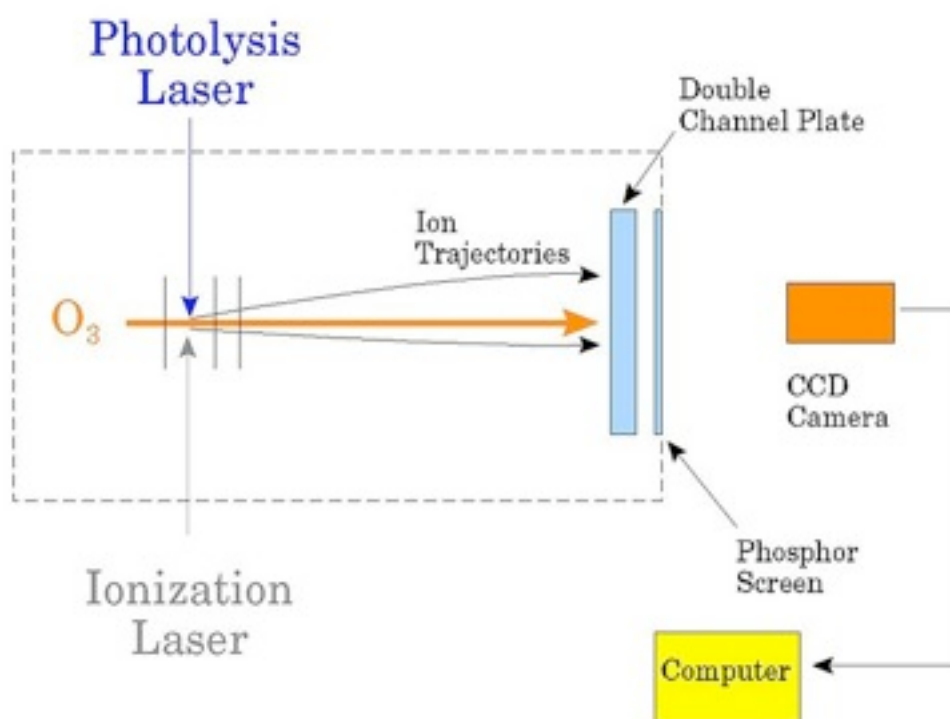


fig 3: The experimental set up is shown in the figure and as we already mentioned two crossed beams , a molecular beam and a laser beam create ions which are accelerated in a time-of-flight tube (TOF), so ion trajectories are created and finally hitting a detector consisting MCP's and a phosphor screen. Light emitted from the phosphor screen is finally integrated in the CCD camera

To optimize the performance of the velocity map imaging method one needs to improve the spatial quality of the 2D image, since the mapping of 3D distributions of charged particles onto 2D detector is dependent on the electrode configuration used. So we are about to demonstrate the conventional grid electrodes set-up versus three plate electrostatic lens with open electrodes . It shall be pointed how this lens avoid distortions commonly present in imaging with grids. It turns out that the ion lens can be operated such that particles with the same initial velocity are mapped onto the same point on the detector. The heart of velocity map imaging technique is the use of electrostatic lens .

The performance of velocity map imaging requires the following:

1. The cloud of charged particles should be collapsed in one dimension along the TOF axis for each mass formed. This implies minimum spread in time of flight of the cloud so that the mass selectivity and homogeneous detection sensitivity for all particles in the cloud is achieved.
2. The size of the image must be linearly proportional to the expansion speed for any kinetic energy release.
3. Dependencies on shapes and propagation directions of molecular and laser beams should be minimized. This means that any blurring of the image related to the size of the ionization volume should be kept as small as possible.

Several ion optics configurations have been used in the past like , Willey and Mc-Laren set-up,[8], repeller plate with two grid electrodes (extractor and ground), a conventional imaging set-up,[9] , repeller with one grid electrode and

velocity map imaging set-up[10],[11] , repeller with open extractor and ground electrodes.

The first configuration it has proven to be useful with time of flight, yielding in a high mass resolution by space focusing. However two grids distort the ion trajectories to a large extent and reduce the transmission.

Also commonly applied in imaging applications is the single-grid set-up. By reducing the number of grids less distortion to the ion/electron trajectories appears and a higher transmission is achieved. Although , deviations of the trajectories still occur and the image still is blurred.

Finally in the velocity map imaging set-up, using open lens electrodes the problems are solved. 100% transmission is reached and trajectory deflections will not occur. By making use of open electrodes the equipotential surfaces are bent and can be adjusted by changing the extractor voltage. In this way the electrode configuration act as an electrostatic lens.

Applying this configuration less distortions occur and the images are focused sharply on the imaging detector plane for any length of the time -of -flight tube.

In the next figure the difference is shown.

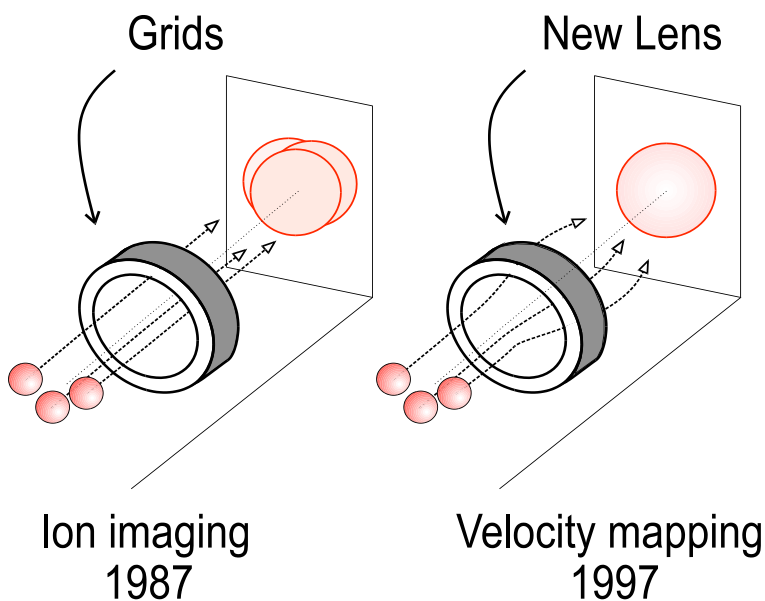


fig 4 : ion imaging versus velocity map imaging is shown, also the distortions in images are shown

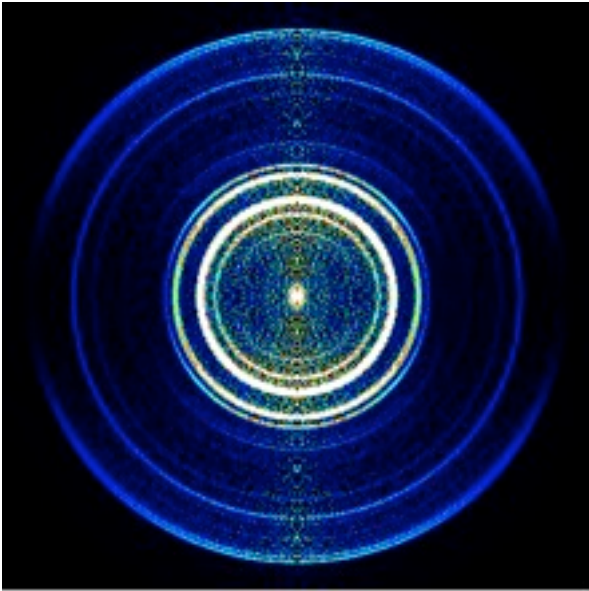


Figure 5: an image of  $O^+$  ions from dissociation at 225.0 nm is shown.[13]

### **1.3 Coherent Control**

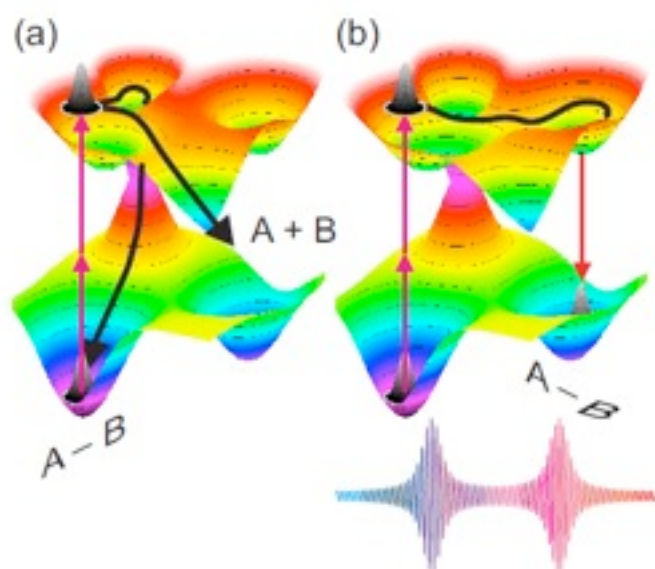
In this section coherent control is discussed. Coherence in physics is a property of waves that enables stationary interference. More generally, coherence describes all properties of the correlation between physical quantities of a wave.

Coherent control is very popular in chemical dynamics as it can control a chemical reaction usually by using a shaped ultrashort laser pulse. By exciting one bond, the bond vibrates. However few fs later the entire molecule vibrates. Long pulses excite the entire molecule and the weakest bond breaks, no matter which bond was excited. In contrast with ultrashort laser pulses which have the ability to localize the energy in the bond of interest. With coherent control in combination with ultrashort laser pulses we can vibrate a molecule in a such a way as to break the bond of interest.

When interfering, two waves can add together to create a larger wave (constructive interference) or subtract from each other to create a smaller wave

(destructive interference) , depending on their relative phase. Two waves are said to be coherent if they have a constant relative phase. [13]

Coherent control is a quantum mechanical based method for dynamical processes with light, employing quantum interference phenomena which are controlled by shaping the phase of laser pulses [14]



Quantum control strategies making use of tailored ultrashort light pulses are enormously successful to manipulate a great variety of physical and chemical properties of matter.

The operating system of chemical reaction control is shown in the next figure.

fig 6 : operating principle of coherent control exerted on photochemical reaction involving the ground and excited state Potential Energy Surface(PES) of a molecule A-B. (a) example of reaction pathways on the unperturbed excited state PES (b) a new pathway on the PES modified by the interaction with a shaped strong laser field (bottom) gives rise to a reaction channel inaccessible in weak laser fields.

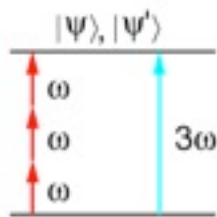
Upon excitation, a wave packet is created in the excited potential energy surface (PES) of a molecule AB. Multiple pathways (a) such as dissociation , relaxation via conical intersections are available to form sometimes unwanted reaction products or dissipate the excitation energy. To steer this process coherent control schemes have been devised to manipulate the initial position and momentum of the excited state wave-packet in order to select one of the

accessible pathways via shaped laser pulses. Strong shaped laser pulses open new pathways by modifying the excited state PES via AC Stark-Shifts as shown in figure (b)..These pathways on the light induced potentials open new reaction channels which are inaccessible in weak laser fields. This combination of pulse shaping( chapter 2) with closed loop adaptive feedback learning algorithms allows to optimize virtually any conceivable observable

In conclusion coherent control in chemistry attempts to control a chemical reaction with light using an ultrashort laser pulse. It is an active broad field of research. One of the most beautiful results of coherent control in combination with ultrashort laser pulses is electron waves as coherent sums of the s,p,d,f wave-functions or watch wave-functions and their contribution by changing the polarization in real time .

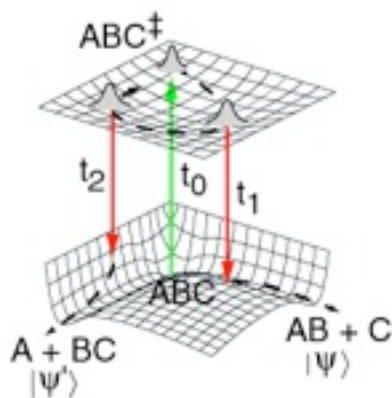
A lot's of simple methods have been developed for chemical reactions. Some of them are the following:

**Brumer-Shapiro**  
"phase control"  
 $\Delta\Phi = \Phi_{\omega} - \Phi_{3\omega}$



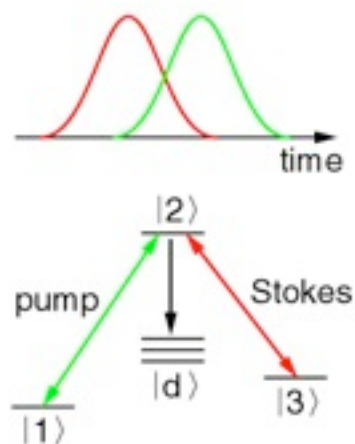
CPL **126**, 541 (1986)

**Tannor-Kosloff-Rice**  
"pump-dump control"  
 $\Delta t = t_{1,2} - t_0$



JCP **85**, 5805 (1986)

**Bergmann et al.**  
"STIRAP control"



CPL **149**, 463 (1988)

fig 7: Brumer and Shapiro, Tannor-Kosloff-Rice , Bergmann et al coherent control schemes

These methods often work but they are not general.

Brumer-Sapiro [15], Tannor-Kosloff-Rice [16] .

### ***Brumer - Sapiro***

Active control in the frequency domain has been beautifully demonstrated by Brumer and Shapiro. They proposed to use two or more continuous wave (cw) fields to coherently interfere with a degenerate molecular doorway state which may lead to two or more final possible outcomes of a reaction.

In the Brumer-Sapiro coherent control scheme, the selectivity of a particular reaction channel is regulated by the relative phase amplitude and polarization of two or more incident continuous wave fields.

This coherent control scheme has been also used experimentally in a lots of studies.[15]

### ***Tannor -Rice -Kosloff***

In this coherent control scheme reaction selectivity is achieved by proper timing of the second (dump) light pulse to coincide with the evolution of a pump-dumped molecule into desired product Frank Condon region. It consists of a simple time domain control which has been performed for several applications. In Tannor-Rice original work, the shape of dump field was also optimized with respect to a fixed pump field in the weak response regime. [16] , [17]

### ***Bergmann at al.***

In STIRAP (stimulated Raman Adiabatic Passage ) coherent control , a method of using partially overlapping pulses (from dump and Stokes laser) to produce complete population transfer between two quantum states of an atom or molecule.

STIRAP is a technique usually used in a three-level atomic systems in interaction with two laser pulses to transfer coherently the atomic population between the two ground states.

Using STIRAP technique all the population can be transferred from one state to another without populating the intermediate state. The high efficiency of this coherent technique has motivated a lots of applications . [18]

## ***Coherent momentum transfer***

In this thesis , momentum transfer via coherent population transfer within magnetic sub-levels induced by linearly and circularly polarized radiation is discussed.

Manipulation of magnetic order requires angular momentum transfer. It has been reported that excitation of a medium with a femtosecond laser pulse results in a large change of angular momentum in magnetic subsystems at the suprisingly fast time scale of the laser pulse.

One photon excitation of rubidium atoms to individual magnetic sub-levels are investigated using linearly and circularly polarized shaped laser pulses and we show that coherence between linearly-circularly polarized waves at different frequencies leads to creation of angular momentum. ( more details in the last chapter)

## References

1. Molecular reaction dynamics, Raphael D. Levine, Cambridge University Press, 2005
2. Reactive and Inelastic Collisions involving Molecules in state selected Vibrational States, by I.W.M. Smith
3. Newton's Spheres , Introduction in Molecular Dynamics, Benjamin Whitaker
4. Velocity map imaging of ions and electrons using electrostatic lenses: Application in photoelectron and photofragment ion imaging of molecular oxygen , Andre´ T. J. B. Eppink and David H. Parker
5. An introduction to quadrupole – time-of-flight mass spectrometry ,Igor V. Chernushevich,\* Alexander V. Loboda and Bruce A. Thomson ,JOURNAL OF MASS SPECTROMETRY J. Mass Spectrom. 2001; 36: 849 – 865
6. An introduction to quadrupole – time-of-flight mass spectrometry,Igor V. Chernushevich,\* Alexander V. Loboda and Bruce A. Thomson ,J. Mass Spectrom. 2001; 36: 849 – 865
7. MICROCHANNEL PLATE DETECTORS JOSEPH LADISLAS WIZA, Nuclear Instruments and Methods, Vol. 162, 1979, 587 to 601
8. W. C. Wiley and I. H. Mc Laren, Rev. Sci. Instrum. 26, 1150 ,1955
9. T. Bergmann, T. P. Martin, and H. Schnaber, Rev. Sci. Instrum. 60, 347, 1989
10. J. W. Thoman, Jr. and D. H. Parker, J. Phys. Chem. 94, 4893 ,1990
11. M. A. Buntine, D. P. Baldwin, R. N. Zare, and D. W. Chandler, J. ChemPhys. 94, 4672 , 1991
12. D.H. Parker and A.T.J.B. Eppink, J. Chem. Phys. **107**, 2357 (1997)
13. Young's Double slit experiment
14. Principles of the quantum control of molecular processes by M.Shapiro and P.Brumer
15. P.Brumer and M. Shapiro, "Control of Unimolecular Reactions Using Coherent Light", Chem. Phys. Lett. 126, 541 (1986).
16. D.J. Tannor, R. Kosloff and S.A. Rice, Coherent Pulse Sequence Induced Control of Selectivity of Reactions: Exact Quantum Mechanical Calculations, J. Chem. Phys. 85, 5805-5820 (1986).

17. Brumer et al. STIRAP control , CPL 149, 463 (1988)

18. R. Unanyan , M. Fleischhauer , B.W. Shore , K. Bergmann , Ž . Optics Communications  
155 1998 144 – 154

# Chapter 2

## Velocity Map Imaging ( describing the apparatus)

### Abstract

In this chapter the apparatus of velocity map imaging for Rb is described. The femtosecond laser Ti:sapphire is illustrated, VMI apparatus and Rubidium oven are described and at last the basics for pulse shaping are demonstrated .

## **2.1 Velocity Map Imaging apparatus (Rb)**

In this section the VMI apparatus used for Rb experiment is illustrated. The set-up is quite different from the VMI set-up described in the first chapter.

A schematic view of the apparatus is shown below.

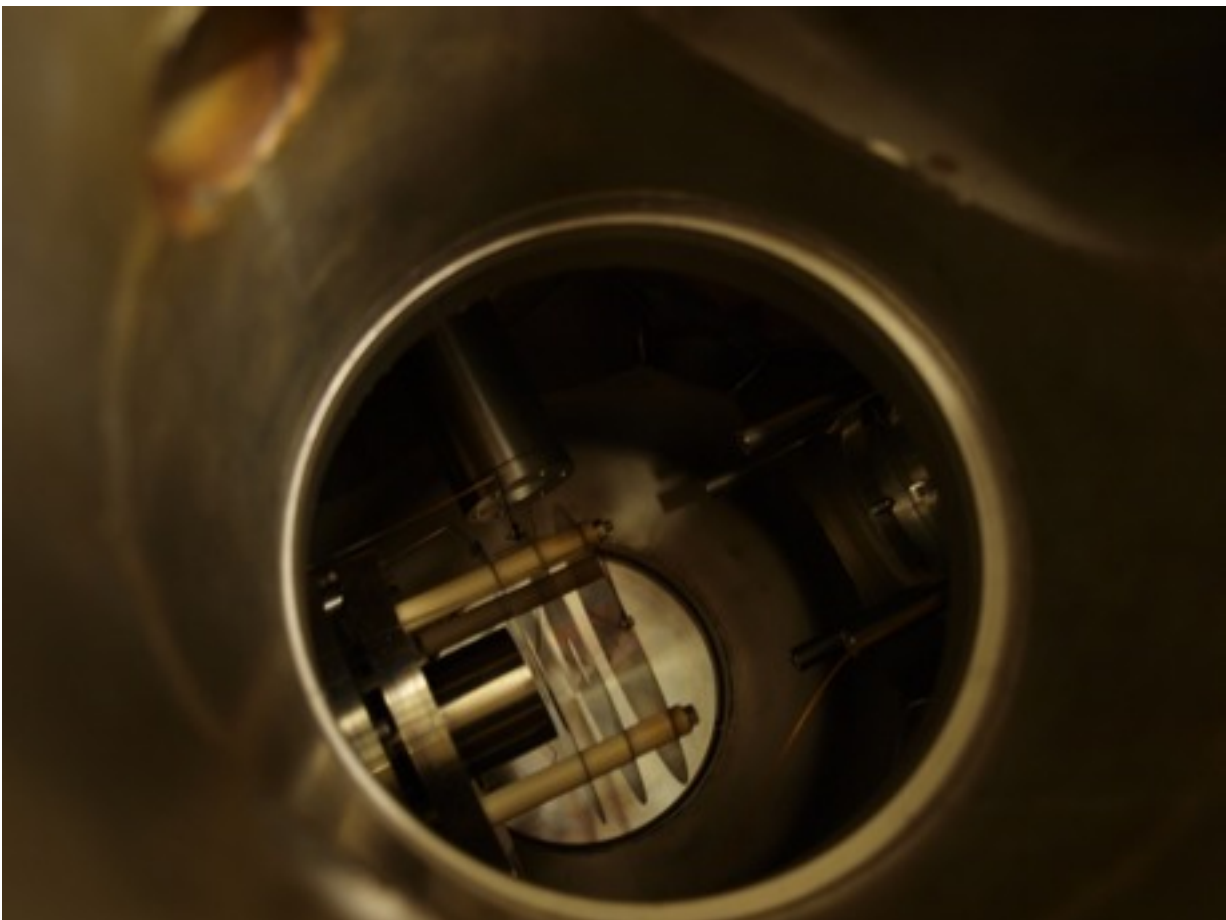


*fig 1 :The experimental setup.*

To carry out our experiments, which are described in the last chapter, we used specific experimental set-up.

It consists of one chamber into which takes place the ionization of rubidium atoms through a rubidium oven. The detection takes place also into the same chamber .

Experiments require high vacuum pressure ( $10^{-6}$  Torr ) in order to avoid undesirable impacts which may affect the results .

### **How Rb atoms are formed?**

Inside the chamber there is a rubidium oven into which a beam of rubidium atoms is formed .

With this design , the aim is to produce the highest possible excited-atom density.

The oven consists of a high temperature emitting source supplied with Rb via capillary action through a tightly wound stainless steel mesh.

A copper crucible surrounds the high temperature emitting source , to collect the most of the emitted Rb into a cool reservoir maintained at just above the Rb melting point.

The high temperature emitting source relies on a temperature gradient between Rubidium's emissive region and the rubidium reservoir.

This gradient is maintained by heating the high temperature emitting source and cooling the crucible.

The crucible temperature is kept at 60 -80 °C well above the 39,5 °C melting point.

High temperatures are avoided to minimize Rb loss and to maintain a low vapor pressure in the reservoir to reduce contamination of the surrounding vacuum chamber .

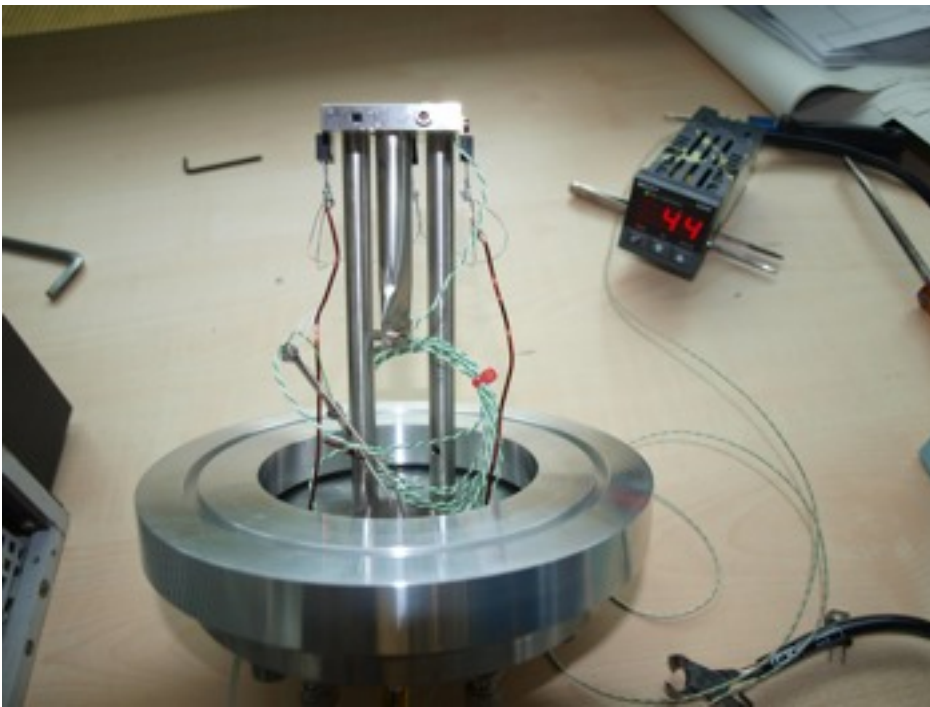


fig 2 : Rubidium oven ( front side)

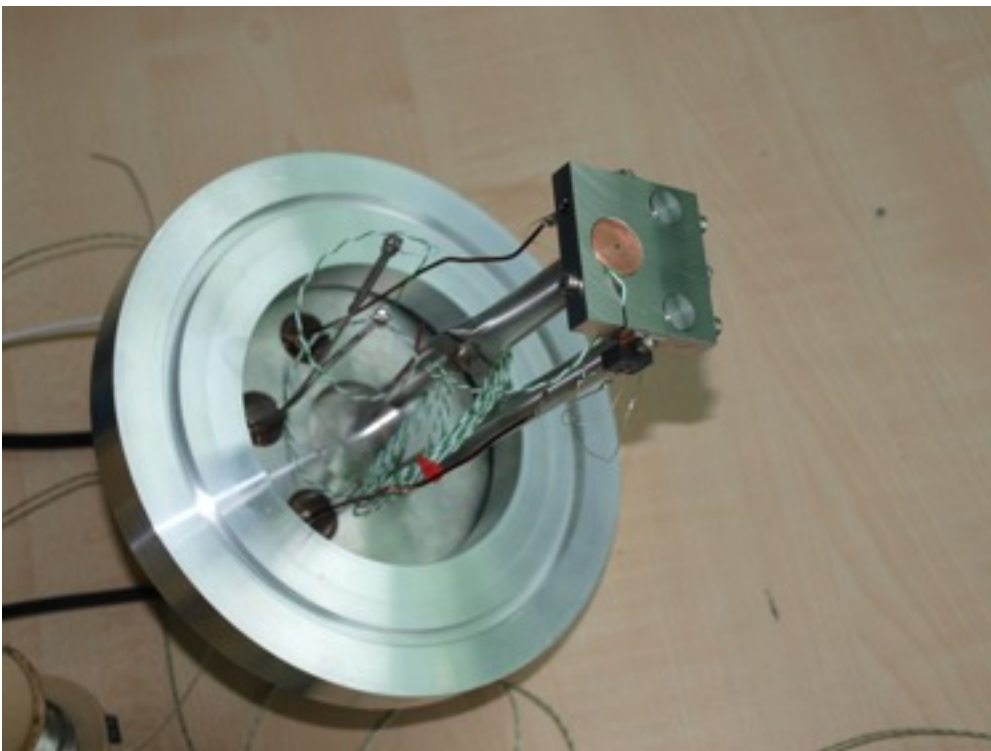


fig 3 : Rubidium oven ( upper side )

Continuing with the experimental set-up , it consists also a gate valve , normally used to produce pulsed molecular beams.

The valve is one hollow cylinder with a screw edge. In the back side of the valve there is MHV connector and a tube for the entrance of Rb.

The electrodes used for this set up is repeller ( R ) , extractor ( E ) , ground electrode (G ) and a phosphor screen, (fig . 1 ) .

The detection of Rb atoms is based on the use of two MCP's ( micro-channel plates) , MCP front and back.

The voltages applied on the electrodes are 2kV on the repeller , 1.8kV on the extractor and 3.5 kV on the phosphor screen , 0.7 kV on the MCP front and 1.5 kV on the MCP back .

Rubidium atoms are projected to a computer which is connected with a high resolution CCD camera.

## **2.2 Femtosecond laser Ti:sapphire**

Femtosecond lasers are illustrated in this section . The ability of femtosecond lasers to induce ultrashort pulses in the order of  $10^{-15}$  sec. is widely applicable

In optics, an ultrashort pulse of light is an electromagnetic pulse whose time duration is on the order of the femtosecond. Such pulses have a broadband optical spectrum and can be created by mode-locked oscillators [4]. They are commonly referred as ultra-fast events.

They are characterized by a high peak intensity, that usually leads to non-linear interactions in various materials.

Ultra-short refers to femtosecond( fs) or picosecond (ps) although such pulses no longer hold the record for the shortest pulses generated. Pulse durations on the atto-second time scale have been reported [5].

Most common femtosecond lasers are the Ti:sapphire lasers also known as Ti:Al<sub>2</sub>O<sub>3</sub> lasers, titanium sapphire lasers or simply Ti:sapphs which are tunable lasers [6] which emit red and near-infrared light in the range from 650 to 1100 nm. These lasers are mainly used because of their tunability and their ability to generate ultrashort pulses.

The types of Ti:sapphire ,

### Mode-locked oscillators

Mode-locked oscillators generate ultrashort pulses with a typical duration between 10 femtoseconds and a few picoseconds.

The pulse repetition frequency is in most cases around 70-90 MHz .Ti:sapphire oscillators are normally pumped with a continuous wave laser beam from an argon or a frequency doubled Nd:YVO<sub>4</sub> laser. Such an oscillator has an average output power of 0.5 to 1.5 Watt.

### Chirped-pulse amplifiers

These devices generate ultrashort, ultrahigh intensity pulses with a duration of 20-100 fs. A typical one stage amplifier can produce pulses up to 5 millijoules in energy at a repetition frequency of 1000 Hz . Usually amplifier crystals are pumped with a pulse frequency doubled Nd:YLF laser at 527 nm to 800 nm.

Two different designs exist for the amplifier , regenerative amplifier and multi-pass amplifier.[7] , [8]

Regenerative amplifiers operate by amplifying single pulses from an oscillator. Instead of a normal cavity with a partially reflective mirror , they contain high-speed optical switches that insert a pulse into a cavity and take the pulse out of the cavity exactly at the right moment when it has been amplified to a high intensity.

### Tunable Continuous wave lasers

Titanium sapphire is especially suitable for pulsed lasers since an ultrashort pulse inherently contains a wide spectrum of frequency components. This is due to the inverse relationship between the frequency bandwidth of a pulse and its time duration, due to there being conjugate variables. However with an appropriate design , titanium sapphire can also be used in continuous wave lasers with extremely narrow linewidths tunable over a wide range.



Titanium -doped sapphire  $Ti^{+3}$  , is widely used transition metal -doped gain medium for tunable lasers

fig 2: Ti sapphire crystal

### Properties of Ti:sapphire

- ◆ Sapphire ( mono-crystalline  $Al_2O_3$  ) has an excellent thermal conductivity, alleviating thermal effects even for high laser powers and intensities.
- ◆  $Ti^{+3}$  ion has a very large gain bandwidth allowing the generation of very short pulses and also wide wavelength tunability. The maximum gain and laser efficiency are obtained around 800 nm. Possible tuning range is 650 nm to 1100 nm but different mirror sets are normally required for covering this huge range
- ◆ There is also a wide range of possible pump wavelengths which however are located in the green spectral region.

In most cases, several watts of pump power are used , even 20 watts. Originally Ti:sapphire lasers were pumped with 514 nm argon ion lasers which are powerful but very inefficient.

Other kinds of green lasers are now available and frequency doubled solid state lasers based on neodymium doped gain media. The pump wavelengths typically 532 nm .

◆ The upper state lifetime of Ti:sapphire is short (3.2  $\mu\text{s}$ ) and the saturation power is very high. This means that the pump intensity needs to be high, so that a strongly focused pump beam and then a pump source with high beam quality is required.

◆ Despite huge emission bandwidth, Ti:sapphire lasers have relatively high laser cross sections, which reduce the tendency of Ti:sapphire lasers for Q-switching.

[9]

### Pulse generation

Ultrashort pulses from Ti:sapphire lasers can be generated by passive mode-locking[10] usually in the form of Kerr lens[ 11] mode locking [12] (KLM)

The combination with a SESAM [13] (semiconductor saturable absorber mirrors ) [13] allows self-starting pulse generation.

A pulse duration around 100 fs is easily achieved . For a high performance it's essential to introduce very precise dispersion compensation with double chirped mirrors.

Typical output powers of mode-locked Ti sapphire lasers are on the order of 0.3 -1 W . A typical pulse repetition rate is 80 MHz.

## Our Femtosecond laser

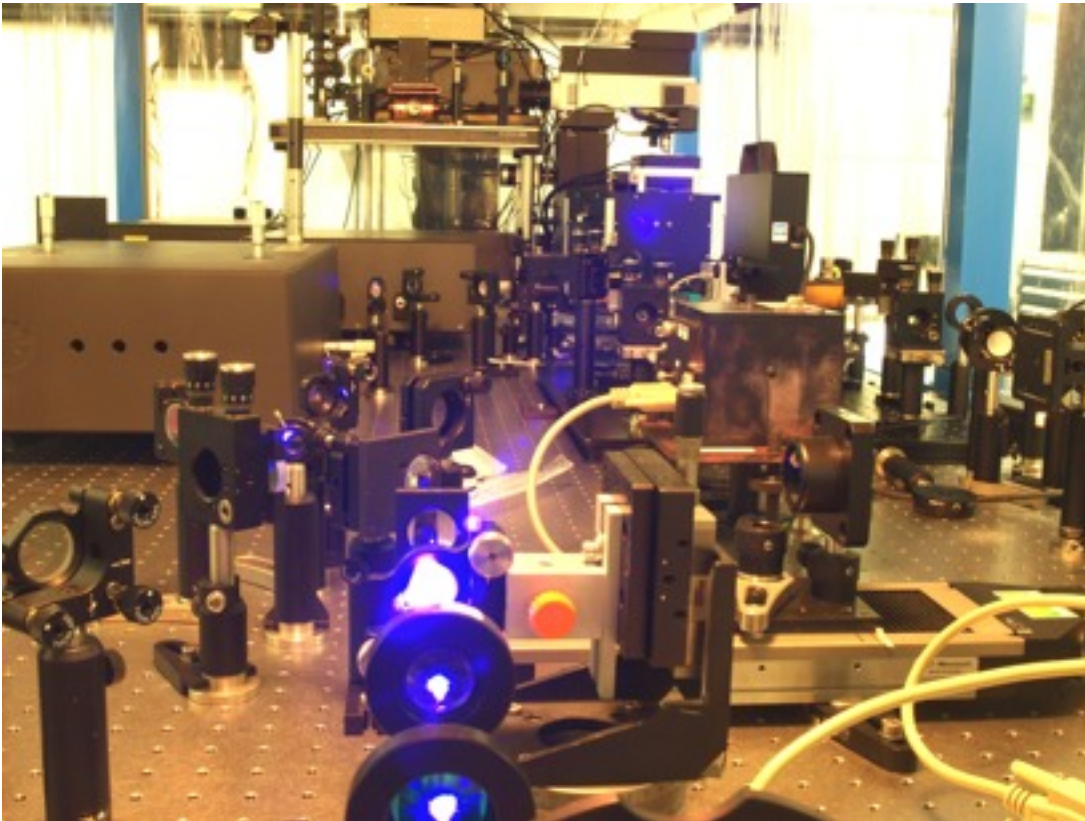


fig 3: In the scheme our femtosecond set-up is illustrated.

The femtosecond Ti:sapphire laser used for this work consists of:

- 1) a pump laser, Verdi. Its a continuous wave solid state laser , operating at 532 nm , which induces output power to 18 W. It is used primarily in Ti:sapphire oscillator pumping application. It is characterized from low optical noise, ( $<0.03\%$  rms ) which makes it the highest pump diode-to-green efficiency pump laser. With the AAA( aluminum free active area) diode modules located inside the power supply and delivering pump light via a patented single core pump fiber to the laser head the resulting homogenized pump beam profile provides superior beam quality during the entire lifetime of the pump module. The beam diameter is  $2.25 \pm 10\%$  mm and the polarization is vertical.
- 2) It consists also from an oscillator: Micra -18 Ti:sapphire oscillator. Micra oscillators are compact and they provide a broad spectral bandwidth.

Featuring an integrated Verdi pump laser, these oscillators are available in three pump power configurations 5W, 10W , 18W . The Micra 18 is a special configuration that provides both the mode-locked beam and a separate green pump beam for applications such as continuous wave pumping of our Reg A regenerative amplifier(next section). It is characterized from average mode-locked power less than 350 mW at 800 nm and CW(continuous wavelength ) output power less than 12W. The beam diameter is 0.5 mm .

- 3) The configuration also consists from a pulse compressor, which can be considered as an oscillator accessory of the oscillator. Pulse compressors temporally compress the broadband pulses from the oscillators ( Micra -18 ) enabling operation very close to the transform limit. By adding Group Velocity Dispersion( GVD) , pulse compressors also allow to pre-compensate for the dispersion introduced when downstream optics are added in order to shorten the pulse width at the sample. For Micra -18 the pulse compressor used is SPO-2 .
- 4) The last part of the laser is an amplifier used to amplify the beam. Here a Reg A 9050 , regenerative amplifier is used. It is a high repetition rate femtosecond Ti:sapphire amplifier. It is a continuous wavelength regenerative amplifier with repetition rate up to 300 kHz. The Reg A 9050 provides a unique range of performance for Ti:sapphire amplifiers. It's CW pumping stable , near diffraction limited output beam with energy  $>3 \mu\text{J}$  at 250 kHz . At this high repetition rate data acquisition is faster. Reg A 9050 is designed to amplify seed pulses from Micra ultra-fast oscillators. For oscillator/amplifier split-pump beam configurations the specified pump laser for Reg A is Verdi . The Micra 18 which intergrates the seed oscillator and an amplifier pump into one package, forms the most compact configuration. Reg A 9050 uses one unit for the amplifier and a second unit for the strecher and compressor. Each pulse energy is up to  $6 \mu\text{J}$  and the average power is 1.5 W. For a typical Reg A 9050 the pulse width is 80 fs. [14]

## **2.3 Pulse shaper**

Nowadays , creating ultrashort pulses in the picosecond and femtosecond range, is really important.

Focus, on this thesis is femtosecond pulse shaping. Over the past decade powerful optical waveform synthesis ( or pulse shaping) methods have been developed.

Femtosecond lasers constitute the world's best pulse generators while pulse shaping is the short pulse optical analog to electronic functions generators which widely provide electronic square waves triangle waves , and indeed arbitrary user specified waveforms.

Here we concentrate on the method , in which waveform synthesis is achieved by spatial masking of the spatially dispersed optical frequency spectrum.

We will be particularly interested in pulse shaping using spatial light modulators (SLM's) , where SLM allows reprogrammable waveform generation under computer control.

### Femtosecond pulse shaping basics

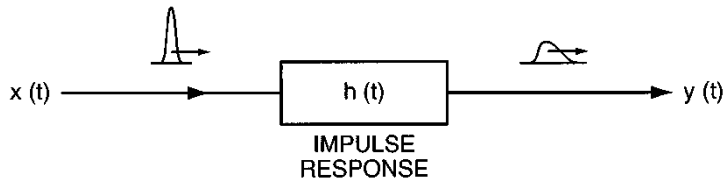
It is based on linear time invariant filter, a concept well known in electrical engineering [15].

Linear filtering is commonly used to process electrical signals ranging from low frequencies ( audio and below) to very high frequencies ( microwave).

We apply linear filtering to generate specially shaped optical waveforms on ps or fs time scale.

Linear filtering can be described in frequency or time domain

(a) TIME DOMAIN



(b) FREQUENCY DOMAIN

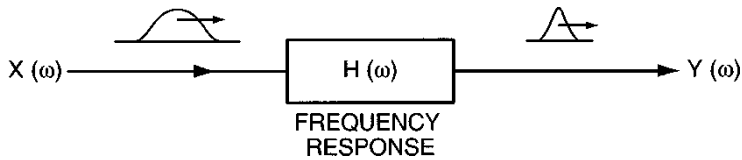


fig 4: pulse shaping by linear filtering (a) time domain view, (b) frequency domain view

The output of a filter is described by the following equation :

$$e_{out}(t) = e_{in}(t) * h(t) ,.$$

Due to Fourier transform relations[16], generation of a desired output waveform can be accomplished by implementing a filter with the required frequency response.

Our pulse shaping approach is described most naturally by means of this frequency domain point of view.

### Pulse shaping apparatus-pulse shaping examples (fixed masks)

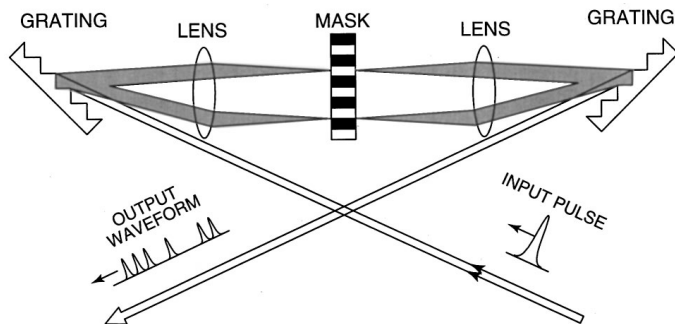


fig 5: basic layout for fourier transform femtosecond pulse shaping

This pulse shaping apparatus consists of a pair of diffraction gratings and lenses arranged in a configuration known as zero-dispersion pulse compressor and a pulse shaping mask. Frequency components contained within the incident ultrashort pulse are angularly dispersed by the first diffraction grating and then focused to small diffraction limited spots at the back focal plane of the first lens, where the frequency components are spatially separated along one dimension.

Essentially the first lens performs a Fourier transform which converts the angular dispersion from the grating to a spatial separation at the back focal plane.

Phase masks are placed in this plane in order to manipulate the spatially dispersed optical Fourier components. After a second lens and grating recombine all the frequencies into a single collimated beam a shaped output pulse is obtained, with the output pulse shape given by the Fourier transform of the pattern transferred by the masks onto the spectrum (absence of the mask the input pulse is identical to the output pulse).

The grating and the lens must be free of dispersion. This can be guaranteed if lenses are set-up as a unit magnification telescope with grating located at the outside focal plane of the telescope.[17]

### Programmable pulse shaping using liquid crystal SLMs (LC SLMs)

We now proceed to discuss programmable pulse shaping using liquid crystal as a programmable mask.

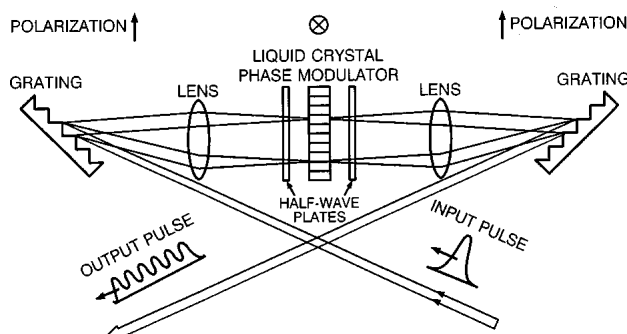


fig:6 programmable pulse shaping using LC SLMs

In the figure above the only difference from other pulse shapers is that instead of fixed masks a liquid crystal is used and a pair of half-wave plates are used to rotate the polarization.

The crystal allows continuously variable phase control of each separate pixel and allows programmable control of the pulse in a millisecond time scale.

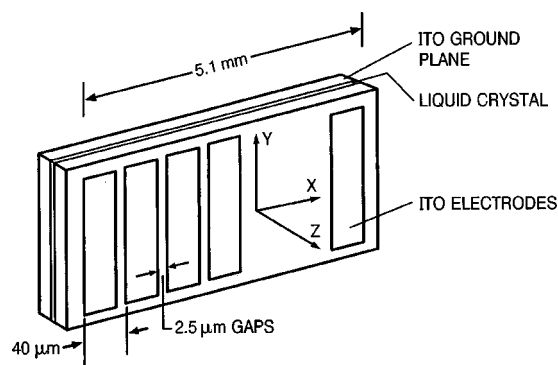


fig 7 :schematic diagram of an LC SLM

The figure above shows an electronically addressed phase only LC-SLM . A thin layer of a nematic liquid crystal is sandwiched between two pieces of glass. The nematic liquid crystal consists of long thin rod-like molecules , which in the absence of an electric field are aligned with their long axes along the y direction.

When an electric field is applied in the z direction the liquid crystal molecules tilt along z axes causing a refractive index change for y- polarized light. A maximum phase change of at least  $2\pi$  is required for complete phase control. In order to apply the required electric field, the inside surface of each piece of glass is coated with a thin transparent, electrically conducting film of indium tin oxide.

## Data measuring of real time pulse shaping

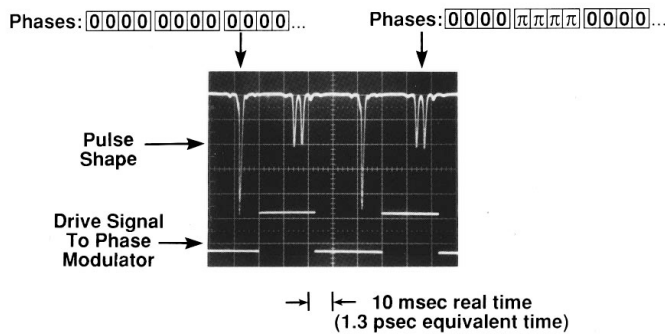


fig 8:real time pulse shaping data

The figure shows real time pulse shaping data measured using an earlier 32 element liquid crystal phase modulator array and 75 fs pulses at 0.62  $\mu\text{m}$  from a pulse mode locked dye laser. In the experiment all the pixels were connected to a constant amplitude drive signal while the other half were switched at a 20 Hz rate between the different drive levels. In one state the phases are all the same and the output is a single pulse similar to the input pulse and in the other state, half of the pixels, experience a relative phase shift of  $\pi$ . [18]

## OUR pulse shaper

Our pulse shaper consists of a liquid crystal LC-SLM and has a 4f line symmetry. [19]

it is composed of two diffraction gratings and two lenses arranges in a 4f set-up with a liquid crystal modulator LCM . Each spectral component is angularly dispersed by the first grating, then is focused to a small diffraction spots in the fourier plane by the first lens. Thus in this plane all spectral components are spatially separated and focused. Then a second combination of lens and grating allows the recombination of all the frequencies into a single collimated beam .

In the next figure the pulse shaper is shown:

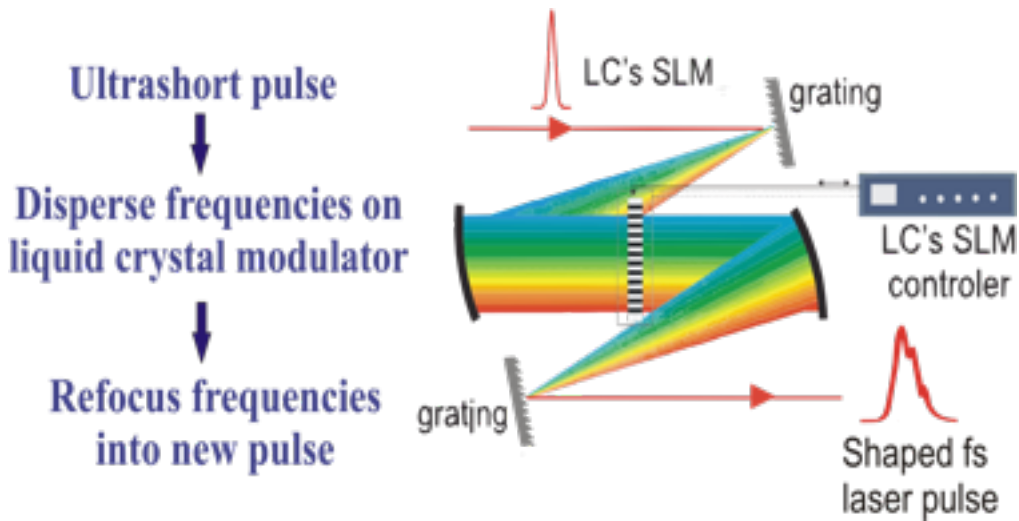


fig 9: pulse shaper , input and output pulse

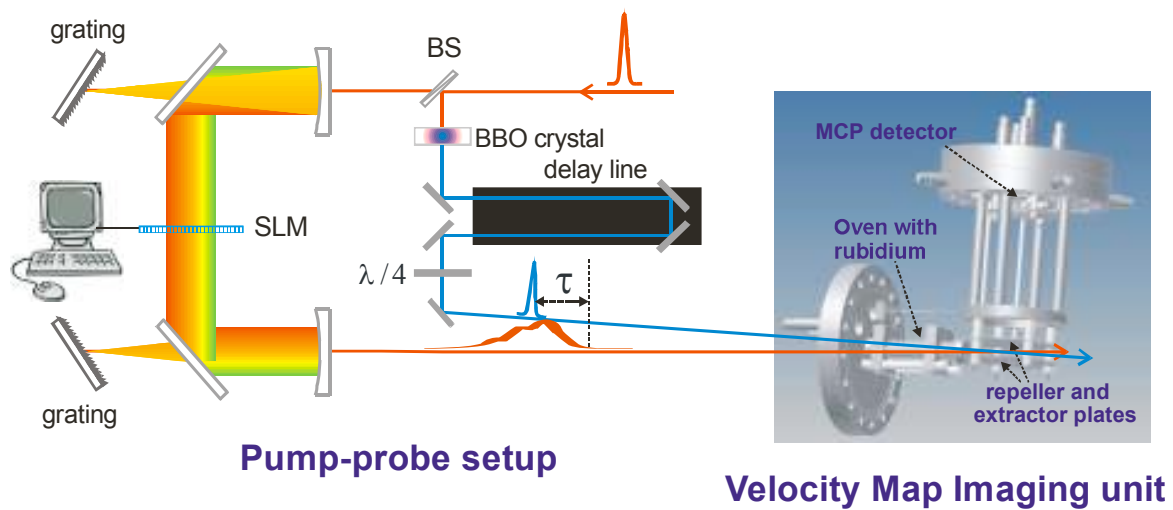


fig 10 : schematic view of experimental set-up

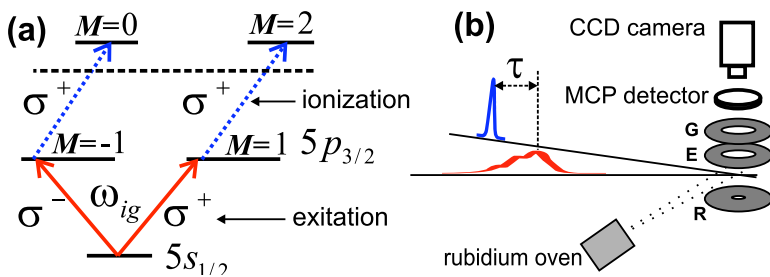


fig 11 : a) the excitation and the probe level system b) schematic lay-out of the experiment

## References

1. Electrostatic lens Systems, D.W.O. HEDDLE , 2nd edition
2. [http://imagine.gsfc.nasa.gov/docs/science/how\\_l2/microchannels.html](http://imagine.gsfc.nasa.gov/docs/science/how_l2/microchannels.html)
3. <http://www.lavision.de/en/products/davis.php>
4. Passively mode-locked Yb:KLu(WO<sub>4</sub>)<sub>2</sub> oscillators,U. Griebner, S. Rivier, V. Petrov, M. Zorn, G. Erbert, M. Weyers, X. Mateos, M. Aguiló, J. Massons, and F. Díaz, Optics Express, Vol. 13, Issue 9, pp. 3465-3470 (2005)
5. <http://www.iesl.forth.gr/downloads/projects/pdf/49.pdf>
6. <http://www.newport.com/images/webdocuments-en/images/11756.pdf>
7. Frequency-Domain Analysis of Super-Regenerative Amplifiers , Jose L. Bohorquez, *Student Member, IEEE*, Anantha P. Chandrakasan, *Fellow, IEEE*, and Joel L. Dawson, *Member, IEEE* , IEEE TRANSACTIONS ON MICROWAVE THEORY AND TECHNIQUES, VOL. 57, NO. 12, DECEMBER 2009
8. New 3D multipass amplifier based on Nd:YAG or Nd:YVO<sub>4</sub> crystals ,SEBASTIEN FORGET<sup>1</sup>( ) , FRANÇOIS BALEMBOIS , PATRICK GEORGES<sup>1</sup>, PIERRE- JEAN DEVILDER<sup>2</sup>
9. [http://www.rp-photonics.com/titanium\\_sapphire\\_lasers.html](http://www.rp-photonics.com/titanium_sapphire_lasers.html)
10. Passive Mode-Locking: Case Studies F. ÖMER ILDAY Department of Physics, Bilkent University, Ankara, Turkey
- 11.Theory of Kerr-lens mode locking: role of self-focusing and radially varying gain Joachim Herrmann , JOSA B, Vol. 11, Issue 3, pp. 498-512 (1994)
- 12.<http://phys.strath.ac.uk/12-370/sld074.htm>
- 13.Semiconductor Saturable Absorber Mirrors (SESAM's) for Femtosecond to Nanosecond Pulse Generation in Solid-State Lasers,IEEE JOURNAL OF SELECTED TOPICS IN QUANTUM ELECTRONICS, VOL. 2, NO. 3, SEPTEMBER 1996
14. <http://www.coherent.com/>
- 15.[http://www.dsprelated.com/dspbooks/filters/Linear\\_Time\\_Invariant\\_Digital\\_Filters.html](http://www.dsprelated.com/dspbooks/filters/Linear_Time_Invariant_Digital_Filters.html)
- 16.<http://www.mathpages.com/home/kmath488/kmath488.htm>
- 17.Femtosecond direct space-to-time pulse shaping in an integrated-optic configuration July 1, 2004 / Vol. 29, No. 13 / OPTICS LETTERS

18. Programmable femtosecond pulse shaping by use of a multielement liquid-crystal phase modulator ,OPTICS LETTERS / Vol. 15, No. 6 / March 15, 1990
19. REVIEW OF SCIENTIFIC INSTRUMENTS VOLUME 71, NUMBER 5 MAY 2000  
Femtosecond pulse shaping using spatial light modulators

# **Chapter 3**

## **Spectroscopy of Rb**

### Abstract

In this chapter, the spectroscopy of rubidium (Rb) is described as it plays an important role to this thesis . Energy level diagrams are illustrated also.

## **Rubidium**

Rubidium is a group IA metal or alkali metal in the 5th period of periodic table. Other members of the group are lithium (Li) , sodium (Na) , potassium (K) , cesium (Cs) and francium (Fr) . [1]



fig1: rubidium crystal

The name of the element comes from the latin word for deepest red , rubidus. The element was discovered by the german chemists Robert Bunsen and Gustav Kirchoff in 1861.

Rubidium is used in vacuum tubes as a getter, a material that combines with and removes trace gases from vacuum tubes. It is also used in the manufacture of photocells and in special glasses. Since it is easily ionized, it might be used as a propellant in ion engines on spacecraft. Recent discoveries of large deposits of rubidium suggest that its usefulness will increase as its properties become better understood.[2]

Rubidium forms a large number of compounds, although none of them has any significant commercial application. Some of the common rubidium compounds are: rubidium chloride (RbCl), rubidium monoxide (Rb<sub>2</sub>O) and rubidium copper sulfate Rb<sub>2</sub>SO<sub>4</sub>·CuSO<sub>4</sub>·6H<sub>2</sub>O).[3]

Rubidium has the following characteristics:

**Atomic Number:** 37

**Atomic Weight:** 85.4678

**Melting Point:** 312.46 K (39.31°C or 102.76°F)

**Boiling Point:** 961 K (688°C or 1270°F)

**Density:** 1.53 grams per cubic centimeter

**Phase at Room Temperature:** Solid

**Element Classification:** Metal

**Period Number:** 5

**Group Number:** 1

**Group Name:** Alkali Metal

Rubidium is the most abundant element in the earth's crust. However it is widely dispersed and not found as the principal component of any mineral. It is a silvery soft, ductile metal, and is the 4th lightest metallic element. It can be a liquid at room temperature (39 C). Like the other alkali metals, Rb metal has a body centered cubic structure

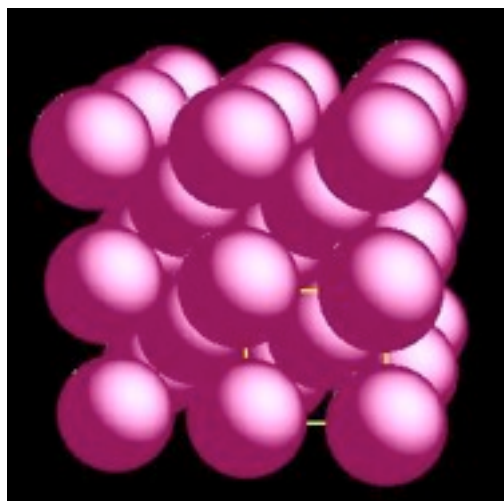


fig 2: rubidium's cubic structure

The chemical and physical properties of rubidium are similar to Cs and K, but is slightly more reactive than K. It reacts rapidly with air. When heated, it ignites spontaneously, burning with a violet flame (like K) and forming four oxides: a yellow monoxide ( $\text{Rb}_2\text{O}$ ); a dark brown peroxide ( $\text{Rb}_2\text{O}_2$ ), a black trioxide

( $\text{Rb}_2\text{O}_3$ ), and a dark orange superoxide ( $\text{RbO}_2$ ). It reacts violently with water (to liberate  $\text{H}_2$  and  $\text{RbOH}$ ).[4]

The uses of the element all depend on the fact that it is highly electropositive, that is, it is an excellent reducing agent. For this reason it has been used as a "getter" - a substance that reacts readily with, and therefore removes,  $\text{O}_2$  - in vacuum tubes. In addition, it is used as the electron source in photocells.

The emission spectrum obtained from rubidium is the following:

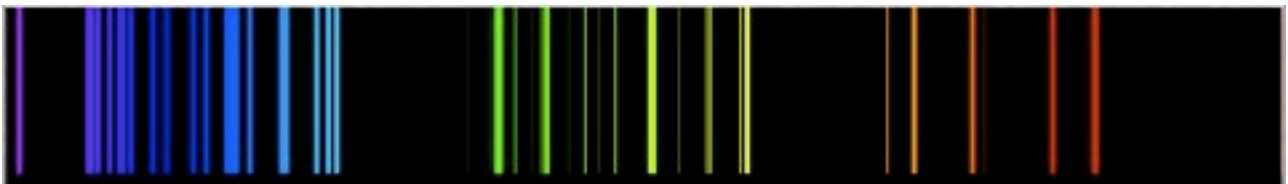


fig 3 : emission spectrum

## **2.1 Spectroscopy of Rubidium**

### Introduction

Atomic physics is an active field of research. Tunable lasers which are used in those experiment provide several milliwatts of optical power and have a typical frequency scanning range of 800 nm .

Several atomic physics experiments have been developed with the basic techniques of laser spectroscopy in order to investigate atomic properties. Recent atomic physics experiment that employ tunable lasers include the spectroscopy of rubidium , the dependence of Doppler-broadening [5] in the absorption spectrum of rubidium , atomic hyperfine structures studies in

atoms , observation of the Faraday effect [6] using the  $D_2$  (next section) resonance line in a rubidium vapor as well.

Doppler-free saturated absorption spectroscopy of rubidium is among the simplest experiments using tunable lasers and the experiment is now widely used in physics laboratories. The single-photon spectroscopy experiment employs a tunable laser tuned to  $5S_{1/2} \rightarrow 5P_{3/2}$  transition ( $\lambda=780.24$  nm ) in rubidium. Saturated absorption spectroscopy of rubidium provides a valuable opportunity to observe the effect of Doppler broadening in atomic spectra and to investigate laser-saturation techniques for extracting the hyperfine structure features of the atomic system. [7] , [8] ,[9] .

An investigation of the  $5S_{1/2} \rightarrow 5D_{5/2}$  two-photon transition in rubidium ( $\lambda=778.1$  nm) is a valuable experiment as it offers the opportunity to directly resolve the hyperfine levels of rubidium without the presence of Doppler broadening. In addition, the experiment provides an opportunity for the direct investigation of relation between laser light polarization, quantum mechanical selection rules, and the observed atomic spectra.

Two photon transitions have been studied using stabilized tunable dye lasers and titanium sapphire lasers. The two photon transitions in rubidium are of particular interest due to their transition wavelength and narrow bandwidth (~ 300 kHz line-width for the two-photon transition. [10]

The optical frequency references have fundamental and commercial applications.[11] , [12]

Commercially, this rubidium two-photon transition is useful for optical communication work . [13]

### **Rubidium's structure**

The ground state electron configuration of Rb is  $1s^2, 2s^2, 2p^6, 3s^2, 3p^6, 3d^{10}, 4s^2, 4p^2, 5s^1$  . Only the valence shell (5s) is unfilled with one electron. As a result the structure of energy levels is similar to that of hydrogen. As for the core  $Rb^+$  ion , it is spherically symmetric , resulting in a total angular momentum (L) , spin angular momentum (S) and thus spin-orbit L-S coupled angular momentum ( $J = |J| = |L + S|$ ) of zero.[14], [15]

Consequently, with all the core ion quantum numbers equal to zero, the observed energy transitions with the associated changes in L-S coupled quantum numbers comes from the valence electron only.

### **Rubidium , ground state**

Stated in L-S coupling notation  $(nl)^{2S+1}L_J$  , ( where n and l are the principle and angular momentum numbers), the ground electronic state is  $(5s^2)S_{\frac{1}{2}}$  . For the ground state  $2S+1 = 2*(1/2) + 1 = 2$  and  $J = |L + S| = |0 + 1/2| = 1/2$  . [16]

### **Rubidium , first excited state**

For  $Rb^+$  ion , from the electron configuration we can see that the first electronic state is found in the  $5p^2$  orbital . Here  $S = 1/2$  and  $L = p = 1 = 1$  , leaving two possible values for J (  $|L-S|$  , ..... ,J,.....,  $|L+S|$  ) equal to 1/2 and 3/2 (doublet).

As a result , two possible energy levels exist for these given n ,l values . The first is less known as less energetic and is called  $D_1$  and has the following quantum numbers :  $(5p^2)P_{\frac{1}{2}}$  . The second, is known as a more energetic excited state, is called  $D_2$  and has the following quantum numbers :  $(5p^2)P_{\frac{3}{2}}$ .

This splitting into two states is known as the magnetic fine structure of an atom where the former corresponds to a transition from the ground state with a

wavelength of 794.8 nm, whereas the latter transition corresponds to a wavelength of 780.0 nm. [17]

**Energy level diagram**

An energy level diagram of the relevant transitions in rubidium are shown in fig. 4 .

a)

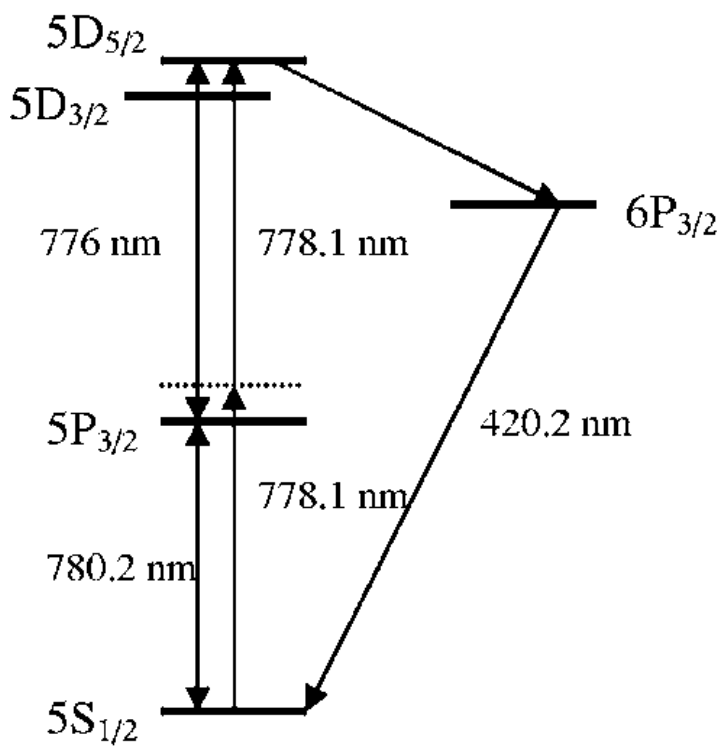


Fig 4 : energy level diagram of the most common transitions in rubidium

The brightest spectral line , corresponding to the  $5S_{\frac{1}{2}} \rightarrow 5P_{\frac{3}{2}}$  ,has a transition wavelength of 780.24 nm ( vacuum wavelength ) and is often used for single-photon transition saturated absorption spectroscopy .

The two photon transition utilizes the  $5D_{5/2}$  excited state which is located 776 nm above the  $5P_{3/2}$  state . Two photon absorption is achieved via the simultaneous absorption is achieved via the simultaneous absorption of the two photons from a single laser tuned to 778.1 nm which excites the electron from the  $5S_{1/2}$  ground state to the  $5D_{5/2}$  excited state . Fluorescence can be also monitored at 420 nm from the  $5D \rightarrow 6P \rightarrow 5S$  cascade decay. [18] , [19] , [20] .

Below the magnetic sub-levels of rubidium are demonstrated from the 5p and the 5d state.

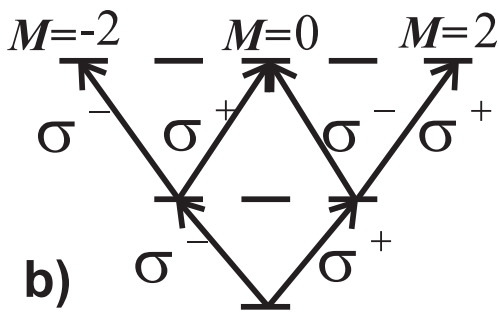


fig 5 : magnetic sub-levels of rubidium

## References

1. [www.webelements.com](http://www.webelements.com)
2. [www.webelements.com/rubidium/uses.html](http://www.webelements.com/rubidium/uses.html)
3. [www.webelements.com/rubidium/compounds.html](http://www.webelements.com/rubidium/compounds.html)
4. <http://www.lenntsch.com/periodic/elements/rb.html>
5. <http://hyperphysics.phy-astr.gsu.edu/hbase/atomic/broaden.html>
6. <http://www.mmresearch.com/articles/article3/>
7. Daril. W. Preston Doppler-free saturated absorption : Laser spectroscopy, Amer. J. of Physics, 64 1432-1436 (1996)
8. Doppler free spectroscopy, Lab handout , MIT(200) Retrieved , 12 Nov 2001 from MIT website , [http:// web.mit.edu/afs/athena/course/8/8.13/ JLExperiments/JLExp-48.pdf](http://web.mit.edu/afs/athena/course/8/8.13/JLExperiments/JLExp-48.pdf)
9. <http://tf.nist.gov/general/pdf/2221.pdf>
10. AbrahamJ. Olson, Evan J. Carlson and Shannon K. Portland, Department of Physics, University of Mayer Portland, Portland , Oregon 97203 (13/1/2006)
11. The European Physical Journal D-Atomic , Molecular, Optical and Plasma Physics, Vol 38 (3) , 545-552
12. [http://Jvsc.JST.go.jp/live/kagadu\\_e/menu.html](http://Jvsc.JST.go.jp/live/kagadu_e/menu.html)
13. <http://www.master-photonics.org/uploads/meta/Ground-Agrawal1.pdf>
14. <http://www.ks-uiuc.edu/services/class/PHYS5480/qm-pdf/chp5.pdf>
15. Optics Letters. Vol 32, Issue 12, pp. 1755-1756 (2007)
16. Chinese Optics Letters, Vol 5, Issue 5 ,pp. 252-254 (2007)
17. Physical Review Letters , Vol.58 , (25) ,22 June 1987
18. Optics Communications, Vol 224 , Issues 4-6 , 1 Sept 2003 , p 247-253

19. American Journal of Physics, Vol.74 , 3 Nov. 2006 , pp. 218-223

# Chapter 4

Ultra-fast coherent control of angular momentum transfer in resonant and off resonant one photon excitation in Rubidium.

## Results and Discussion

### Abstract

In this chapter results on the ultra-fast control of angular momentum in atomic rubidium in a one photon excitation are discussed. It is shown experimentally and theoretically that angular momentum can be controlled on a hundred femtosecond time scale by a polarization-shaped femtosecond laser pulse, only containing linearly polarized frequencies. Transient dynamics of the angular momentum is measured by using velocity map imaging and analyzed by time dependent calculation of Schrodinger equation in the perturbative limit.

## **4.1 Introduction**

Coherent control has become an important area of research of broad interest in both physics and chemistry . [1], [2]

It has been reported that manipulation of magnetic order requires angular momentum transfer. It has been reported also that excitation of a medium with a femtosecond laser pulse results in a large change of angular momentum in magnetic subsystems at the fast time scale of a laser pulse . This time scale is surprisingly too short . Therefore it was suggested that the electromagnetic field directly controls the angular momentum transfer . [3 ] [4] [6] [7]

Normally in an electric dipole transition circularly polarized pulses are required to change the magnetic field number of an electron. In the presence of spin orbit interaction a one photon process probes the magnetization of a medium via the magneto-optical Faraday effect [8]

Detailed understanding of the magneto-optical effects with laser pulses shorter than the time of optical de-coherence is still lacking [9] ,[10] . In solids the problem is bigger with the presence of translational symmetry where the angular momentum is not a good quantum number and optical selection rules are not rigorous.

Angular momentum transfer during off-resonant interactions of light with a simple three level system was first considered by Dudovich et al. [11]

However no possibility of creating net angular momentum in the final state of such a system by a laser pulse with linearly polarized frequencies was considered.

In this thesis we aim to investigate ultra-fast dynamics of the angular momentum in an ideal two-level system, using as a model atomic rubidium. In particular using velocity map imaging we monitor the electron distribution of the

excited state in a one-photon transition  $5s-5p$ . Employing polarization pulse shaping we demonstrate an effective control of the femtosecond dynamics of the angular momentum in the excited state. It is shown that in a one-photon transition the spectral properties of the excitation pulse play a crucial role in the ultra-fast dynamics of the angular momentum transfer. In resonant excitation the angular momentum dynamics in the excited state does not correlate with the helicity of the excitation pulse. In case of, off-resonant excitation the angular momentum follows momentary polarization of the excitation pulse and can be predicted from the time behavior of polarization.



fig 1 : schematic view of the experimental set-up

The amplified 40 fs laser pulses were generated with repetition rate of 250 kHz from a coherent Reg A 9050 amplifier and centered around 795 nm with a pulse energy of approximately  $4\mu\text{J}$ . Part of the pulse was shaped using a pulse shaper with a so-called 4f geometry, as described Prakelt et al [14]. We applied changes to the phase and direction of the different frequency components. In all experiments part of the spectrum above 784 nm was blocked in the Fourier plane to reduce the influence of the  $5p_{1/2}$  level on the observed angular distributions. The probe ionization pulses at 400 nm were produced from fundamental pulses using a BBO crystal and had duration of 100 fs. In the right part of figure above the drawing of the photoelectron detection scheme is shown. The diffused flux of rubidium atoms was produced in an oven held at  $60^\circ\text{C}$  and positioned about 5 cm from the interaction region. During the experiment the pressure in the vacuum chamber was always below  $10^{-6}$  mbar. The repeller and the extractor plates act as a velocity map imaging lens for the photoelectrons [15]. The photoelectrons were detected by a double micro-channel plate (MCP) detector with a phosphor screen and images were recorded with a CCD camera.

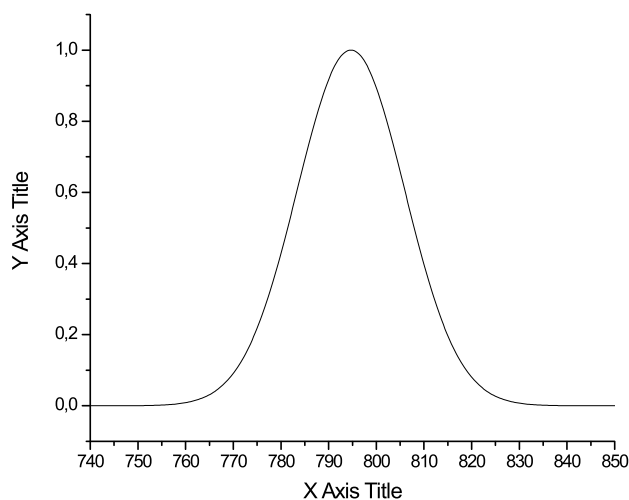


fig:2 laser spectrum centered at 795 nm

In the figure above the spectrum of the laser is illustrated. During the experiment part of the spectrum was blocked in the Fourier plane as mentioned before.

The excitation and ionization laser beams were focused and crossed under a small angle in the interaction region .

## **4.2 Results and discussions**

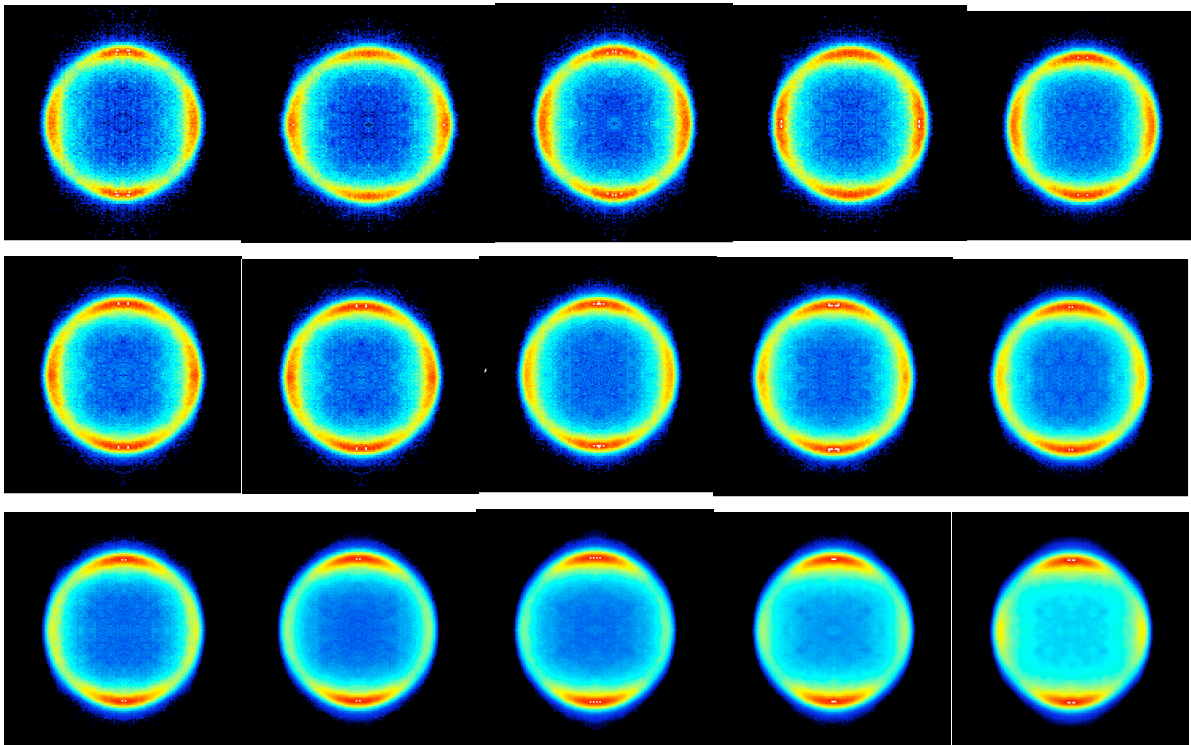
In the next figures the images of the photoelectron angular distributions are shown with the time step of 67 fs . It is clearly seen , that the wave function changes on a 100 fs time- scale , which is determined by the change of the angular distribution in the excited state .

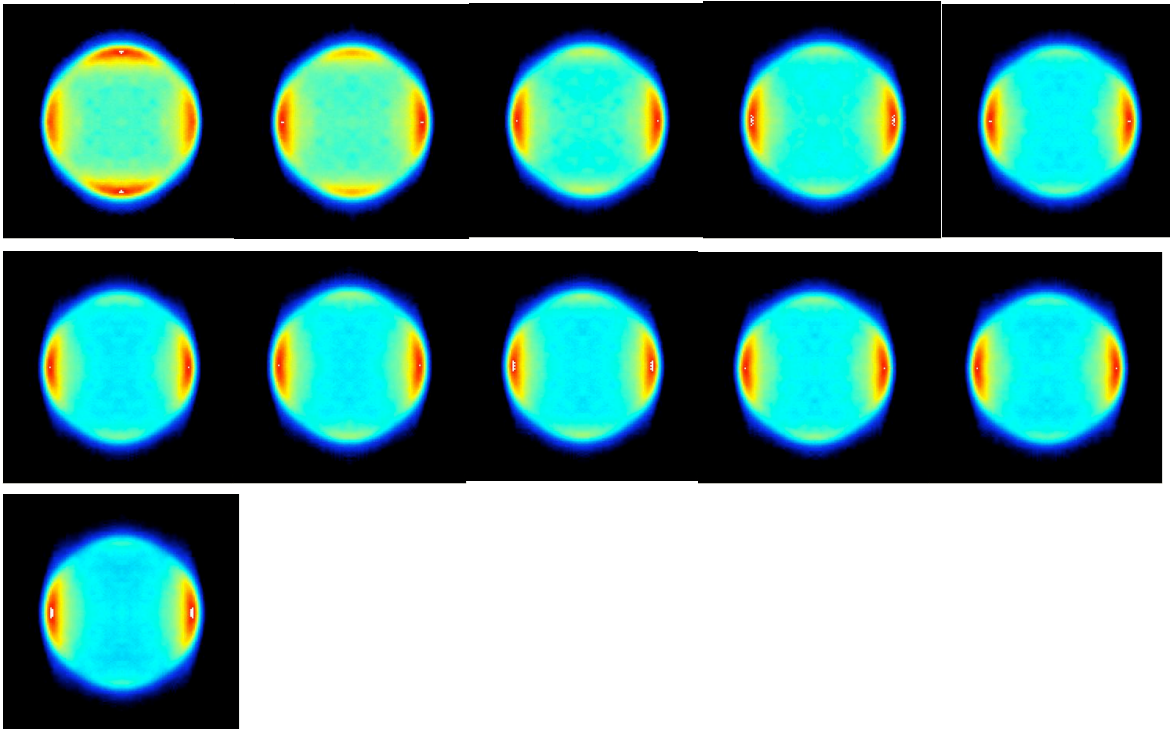
The transient dynamics of the angular momentum transfer in excited 5p state was determined from the photoelectron angular distributions as a function of time delay between excitation and ionization pulses.

The angular momentum in the excited state was reconstructed from the photoelectron images. We performed the analysis in the frame of orbital angular momentum  $L$  , as well as in the frame of total angular momentum  $J$  , taking into account spin-orbit coupling effects .

Typical photoelectron images , obtained during the excitation with polarization shaped pulses are shown in the next figure. The laser beam propagates in vertical direction in the image plane.

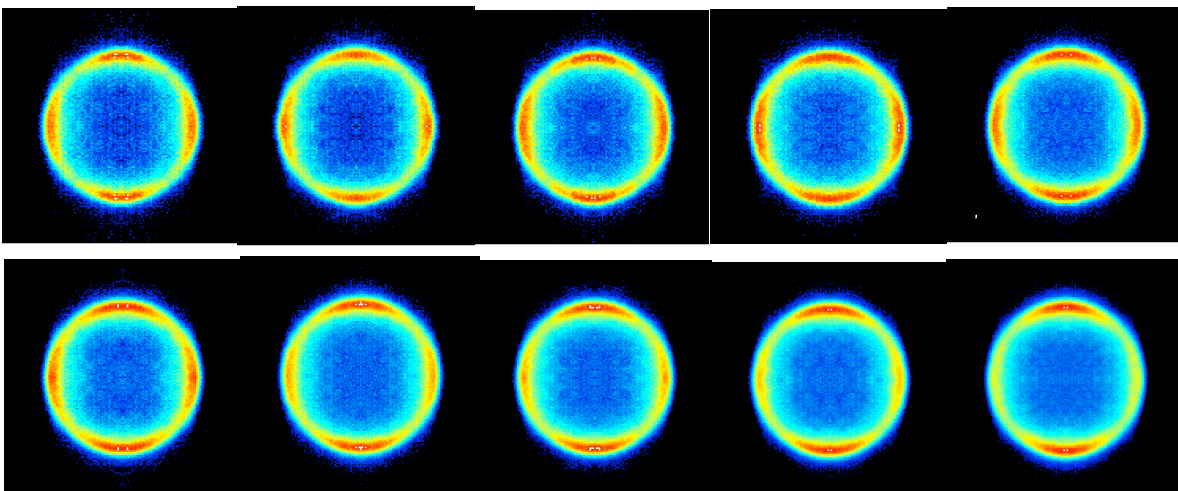
Fig 3 : Set 1, resonance excitation with polarization step applied

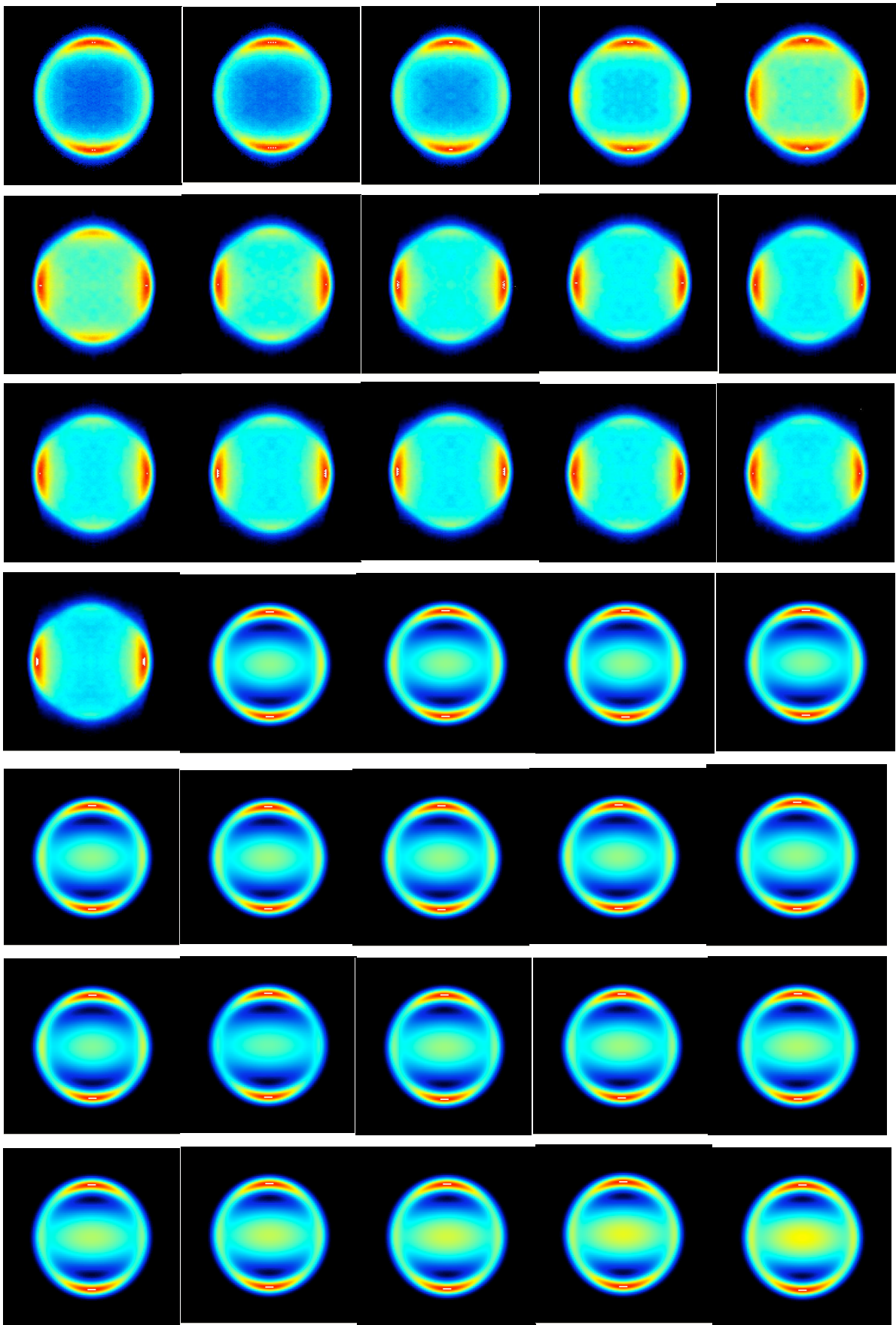


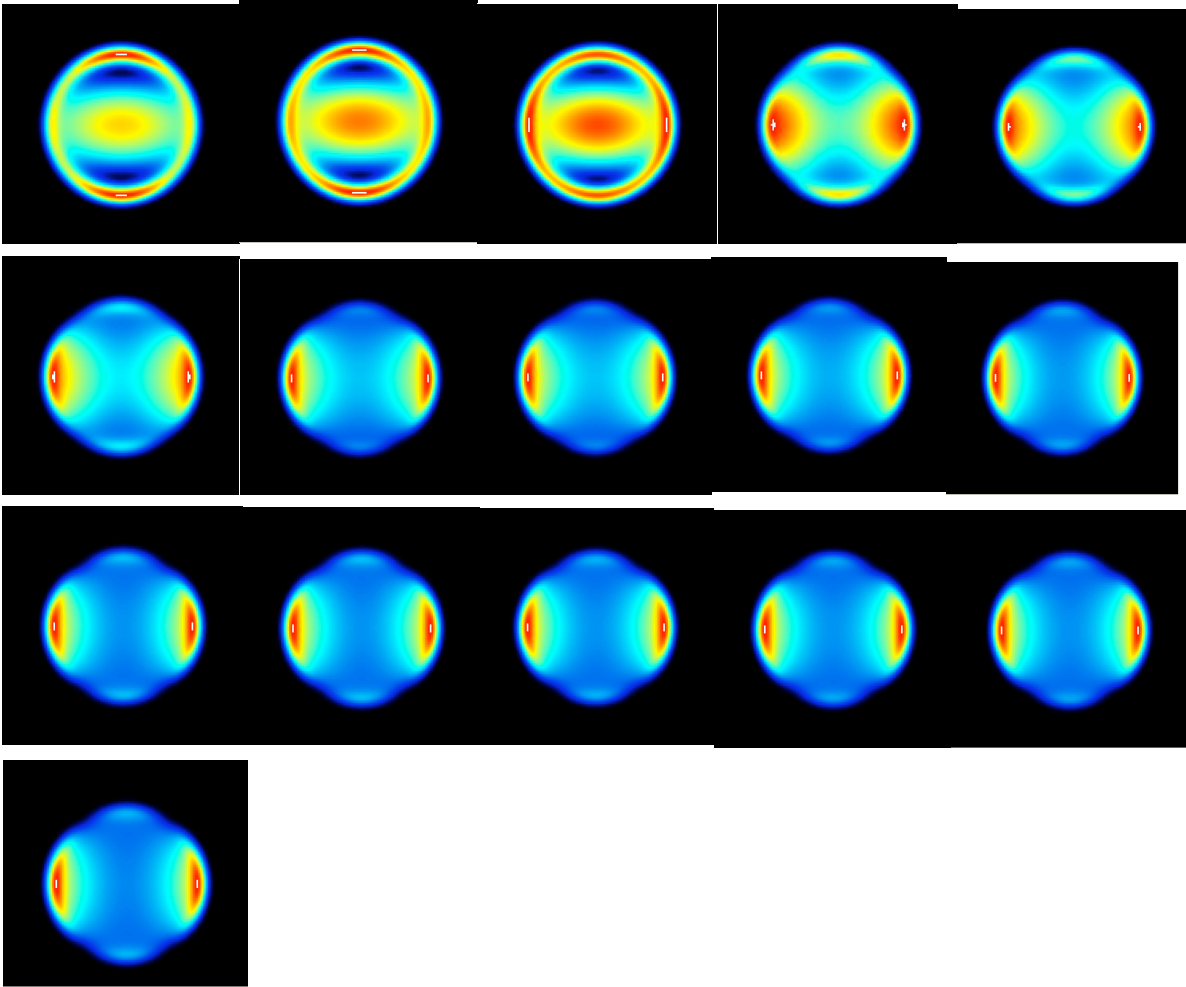


We have monitored the wave-function on real time applying a time step . The images show the photoelectron angular distribution with the time step of 67 fs . Later on , we will clearly see that the electron distribution changes on a 100 fs time-scale , which is determined by the change of the angular distribution in the excited state. The red part on the images shows the part with the most intensity and also indicates the  $\beta$  parameter, anisotropy parameter.

Fig 4: Set 1 gamma, resonance excitation with polarization step and phase step







We apply here a polarization step on our pulse and a phase step also. In this set we monitor the electron distribution and thus the populations at  $m = -1$  and  $m = 1$  magnetic sub-levels are about to be determined. Images with red part (larger intensity) on right and left side represent the situation when both the magnetic sub-levels are populated. The images with the red part on top and bottom represent the  $m = -1$  and the images with the red part on top bottom and left right represent the  $m = 1$ .

The images show photoelectron angular distribution as a function of time during the excitation with polarization shaped pulse.

The change of intensity from the top and bottom to left and right is due to change of polarization from vertical to horizontal.

The main point of this experiment is to monitor, in real time, the electron distribution. Using shaped laser pulses the transition from p orbitals to s

orbitals and d orbitals is observed and plus an effective way to control the angular momentum transfer. Performing further population analysis to the individual magnetic sub-levels of the first excited state of rubidium we investigate a new approach for control the electron distribution. We will prove that the spectral properties play an important role to angular momentum transfer in the first excited state of rubidium. Later on we will relate the off resonance excitation and resonance excitation with the spectral properties. We will demonstrate that in resonance excitation performing further populations analysis in the first excited state of rubidium , the angular momentum transfer can not be predicted from the spectral components of the pulse but instead a phase step should be applied in order those two factors to be related. Conversely in an off-resonance excitation the spectral components can be related with the angular momentum transfer. Angular momentum transfer can be specified completely from the helicity of the pulse can be easily predicted from her.

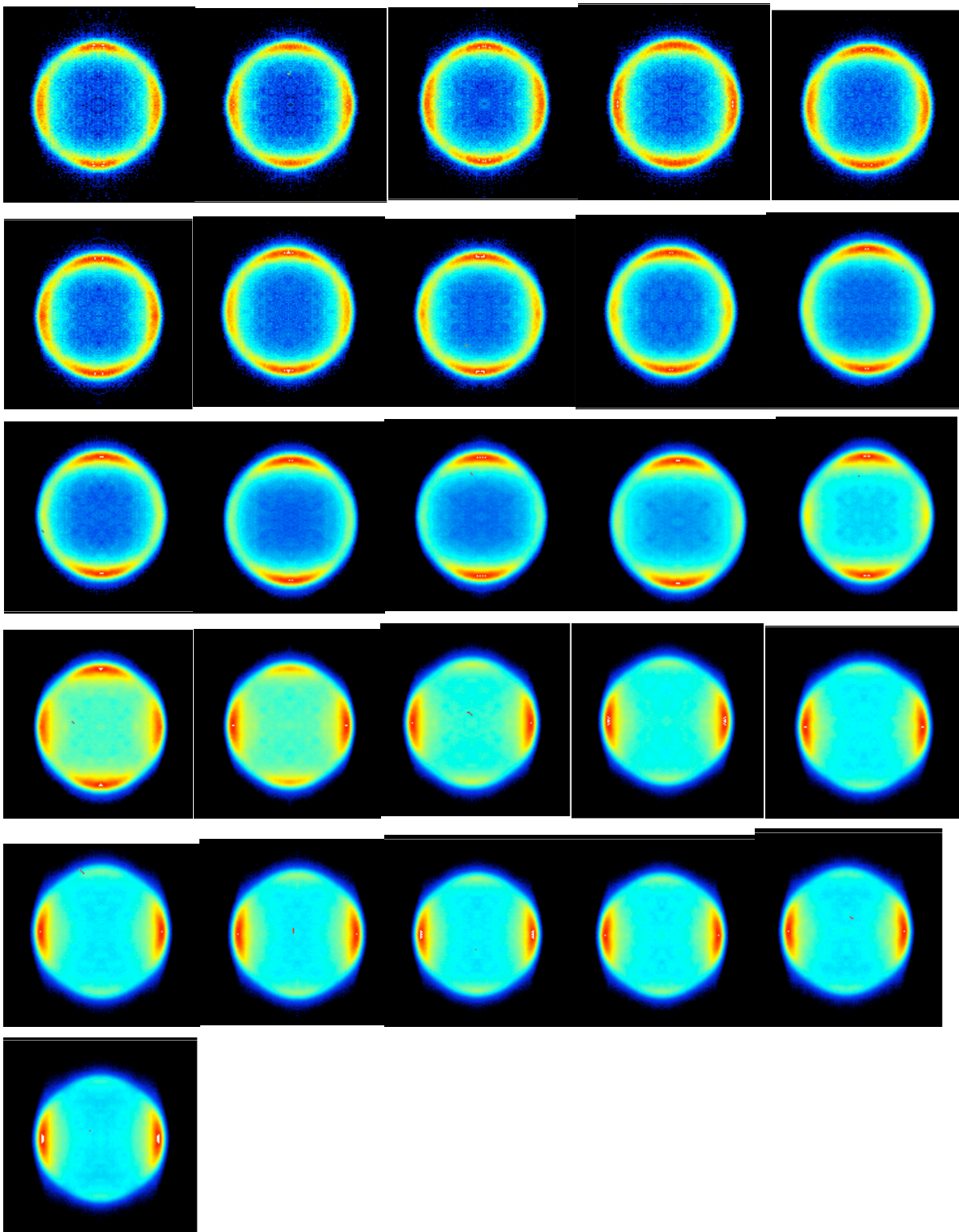
We are now ready to present our results.

In the pictures below the first experimental step is discussed , we discuss for the resonance excitation in which a phase step has been applied to the pulse. In the first row we can clearly see a d -electron distribution which is conserved in the second row also but clearly it is reduced . In the third row the d character is vanished completely and the p-character is induced. In the fourth row a d-character is starting to be induced and a few steps later a different p character is induced.

Until now by applying a simple phase step and a polarization step to our pulse and performing scans and by watching the progress of our signal we have achieved to monitor the change from a d-character to p-character. We have achieved to control so far the electron distribution by applying a phase step.

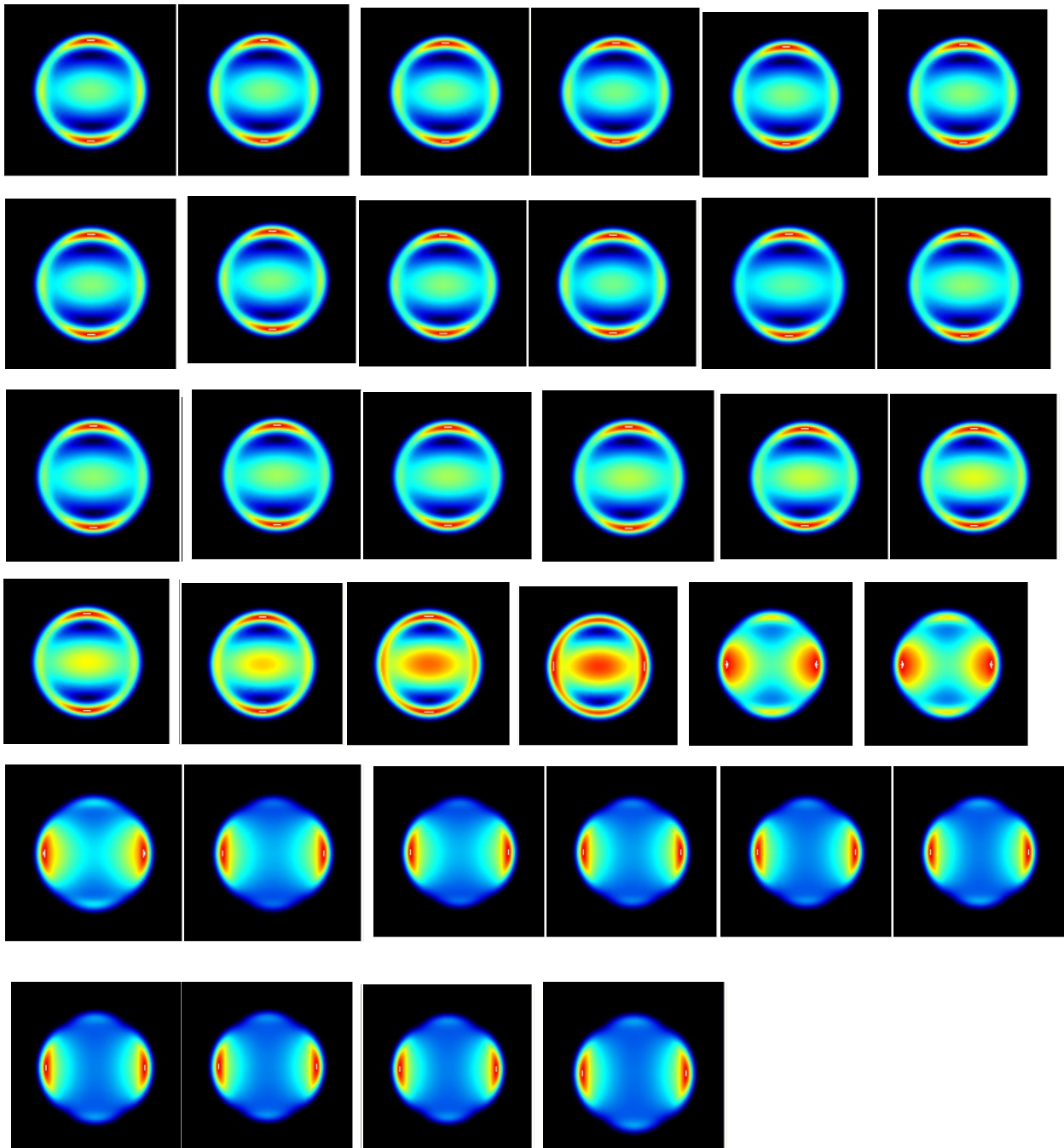
We will see later on that this phase step is not enough by performing further population analysis.

Fig 4 :experimental set- p i



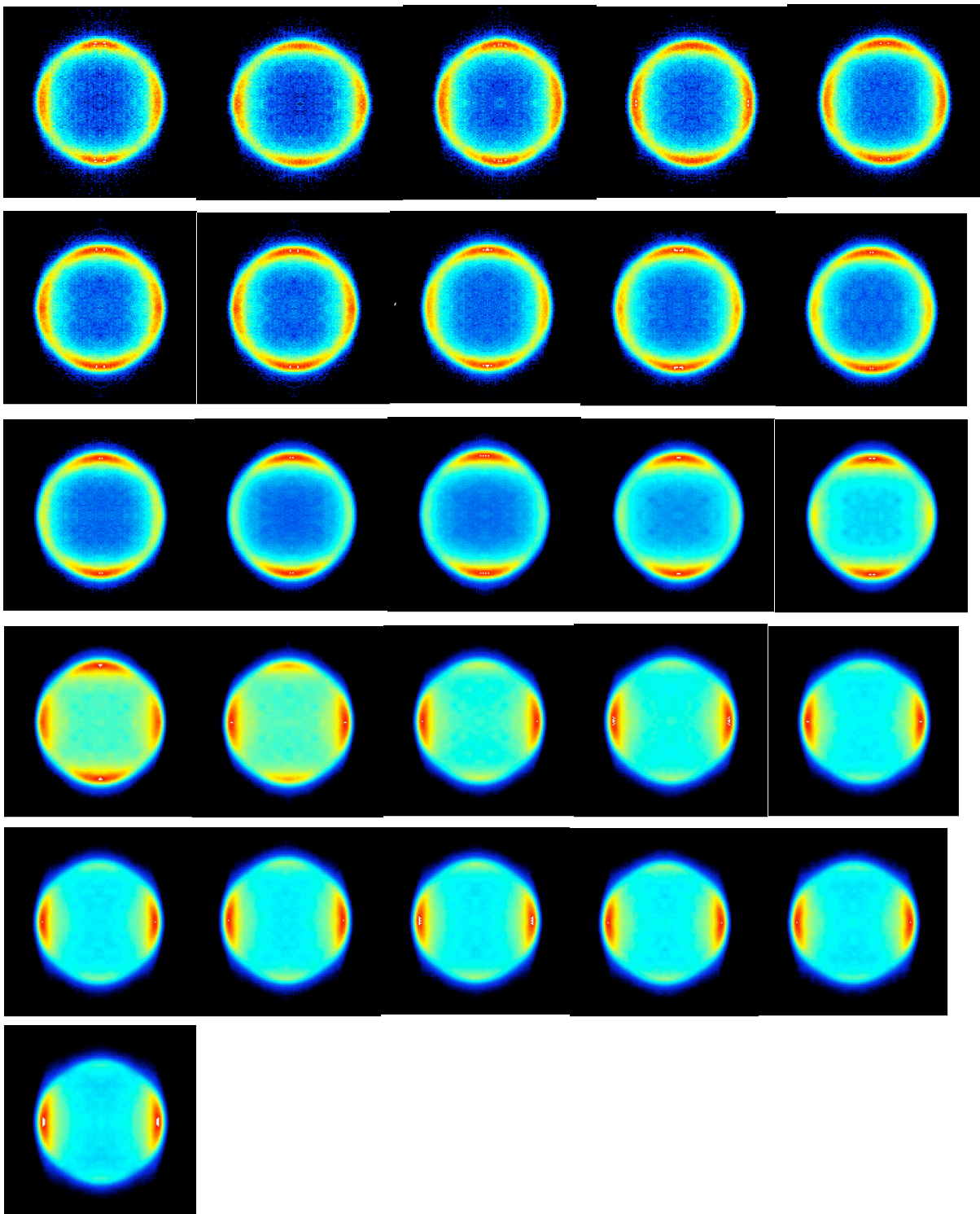
At this point calculated and experimental results are compared. We can clearly see that experimental and calculated results look almost the same with slight differences to the last images.

Fig 5 :calculated set - p i



In the next figure images from the resonance excitation are demonstrated but here we have applied only polarization step meaning that , by changing the polarization of our pulse and performing scans we try to monitor again the different electron configuration and control her.

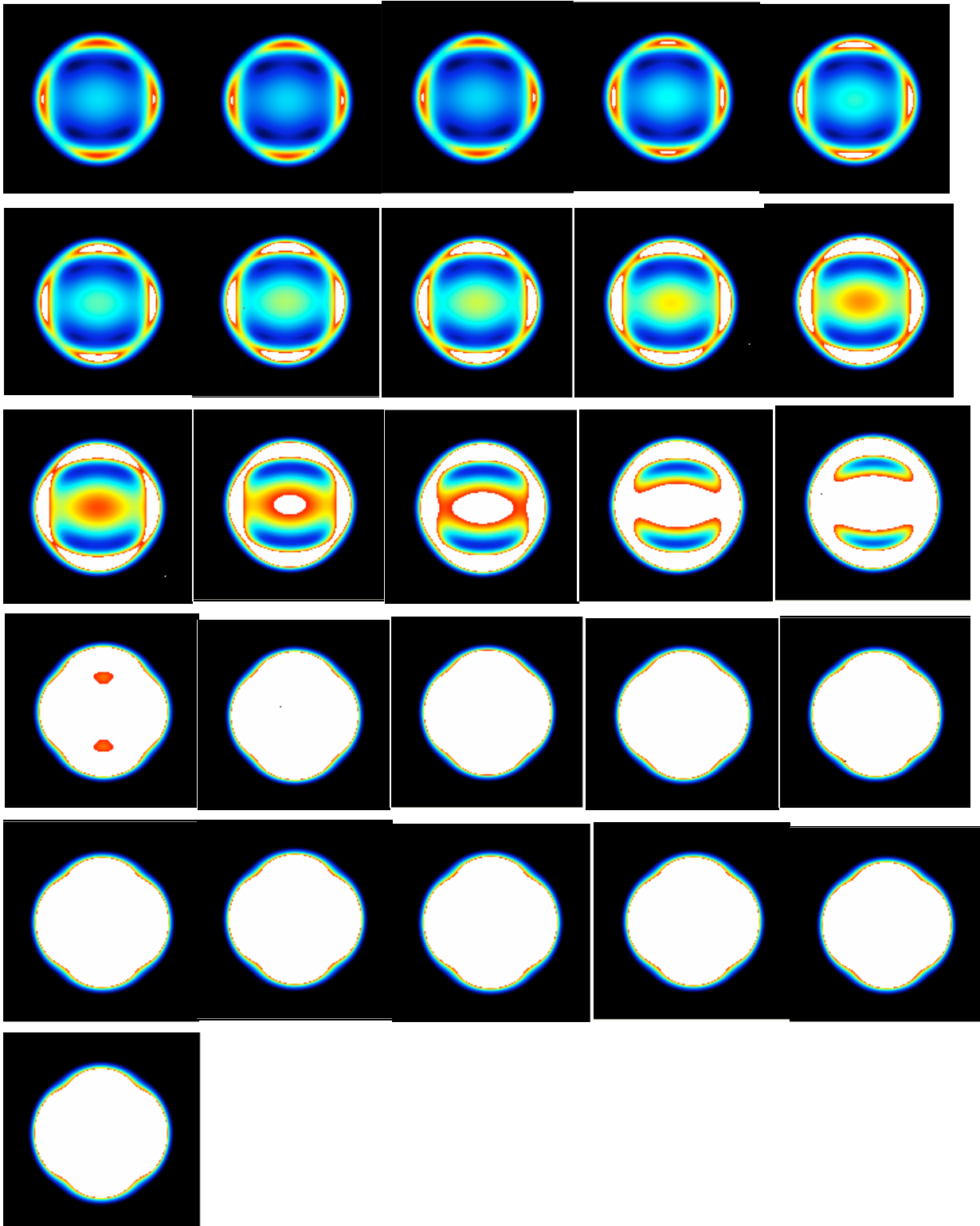
Fig 5 :Experimental set 1



At this point the calculated results are presented for the resonance excitation in which the polarization step only has been applied. We can clearly see that in the first images the calculated and experimental results look the same but at the end those two can not be related. By performing later on population analysis for

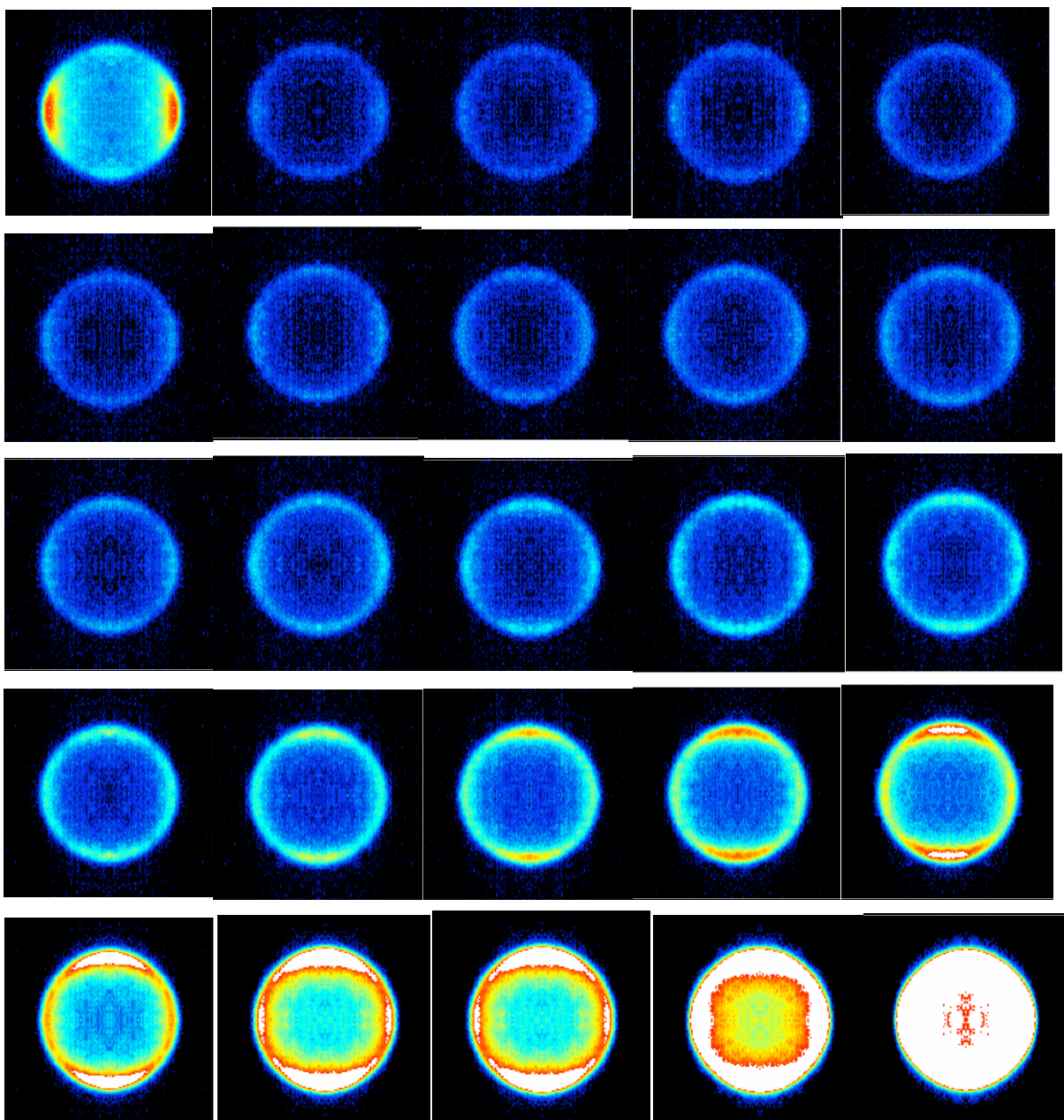
the individual magnetic sub-levels of the first excited state of rubidium we will explain the different appearance of the images

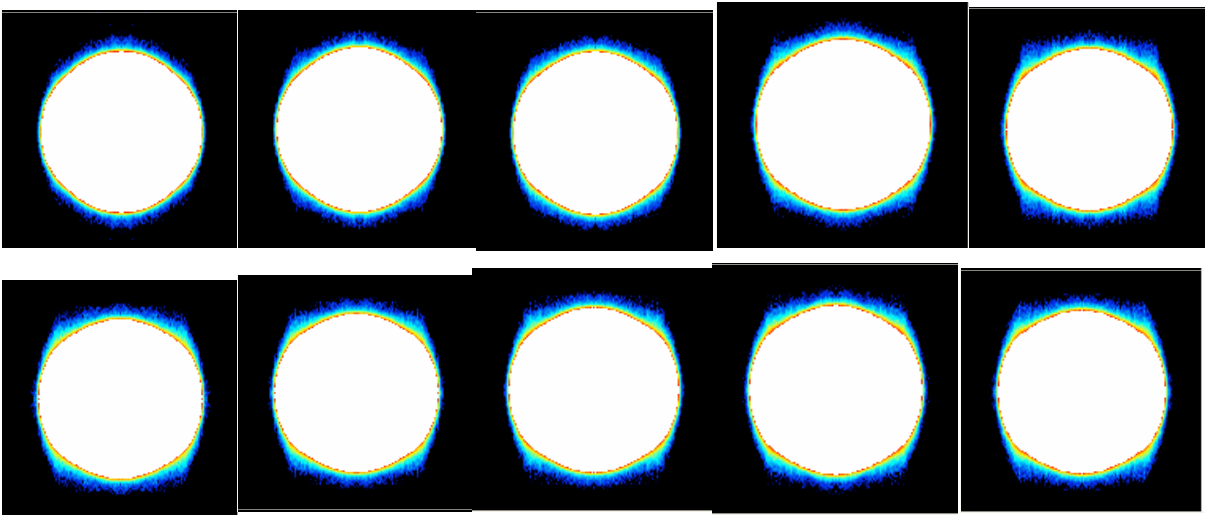
Fig 6 : calculated set 1



We present now results from the off-resonance excitation for rubidium ( 778.1 nm ) . Also here we start from a p-character and by applying a phase step and also polarization we can see the p-character to be reduced and for few images we can see some isotropic spheres and after a few images during our scan we can observe a different p-character, and later on we can observe a d-character to be produced. So far we have achieved also for the off-resonance excitation to control the change of the electron distribution .

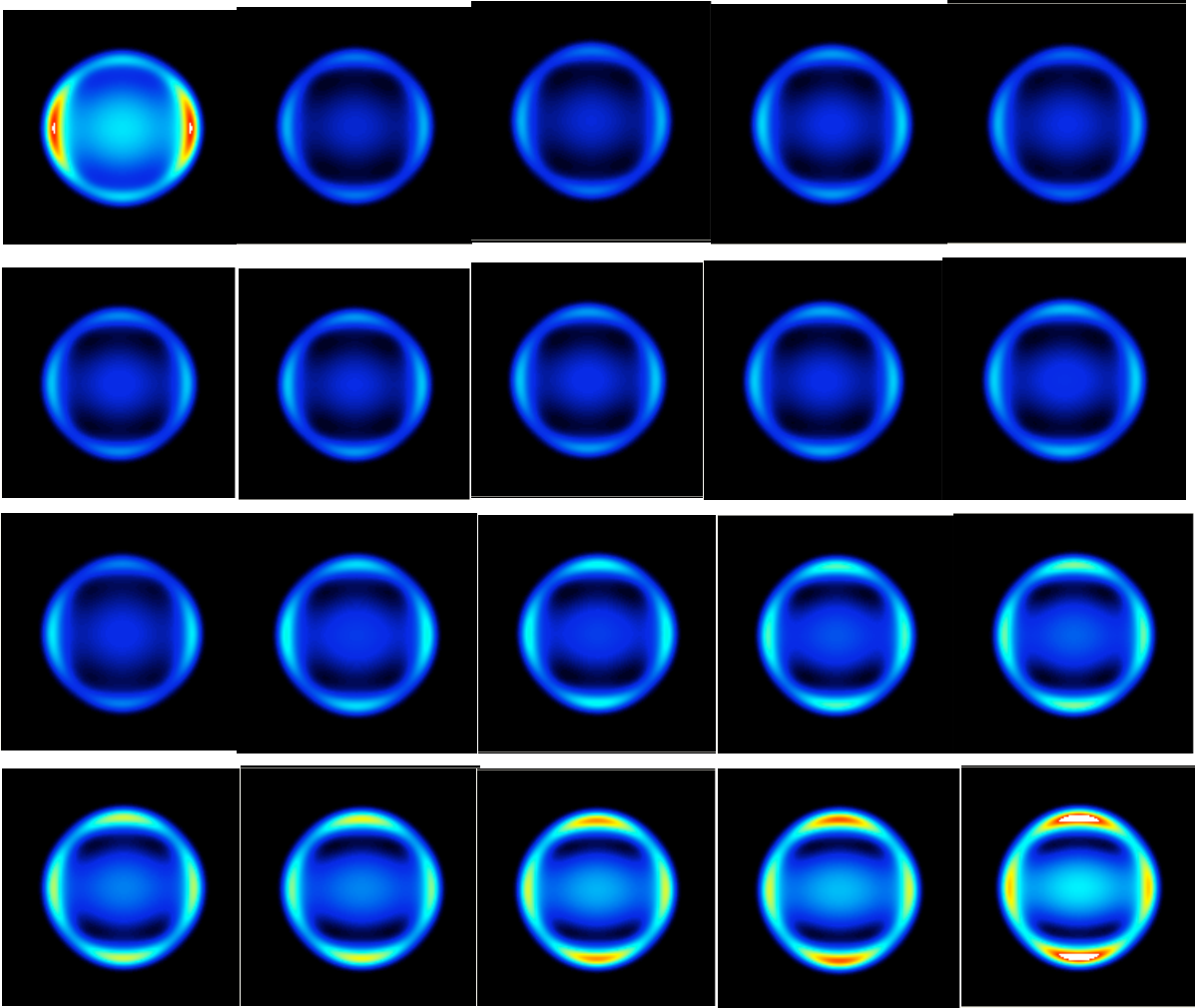
Fig 7 : Experimental P156

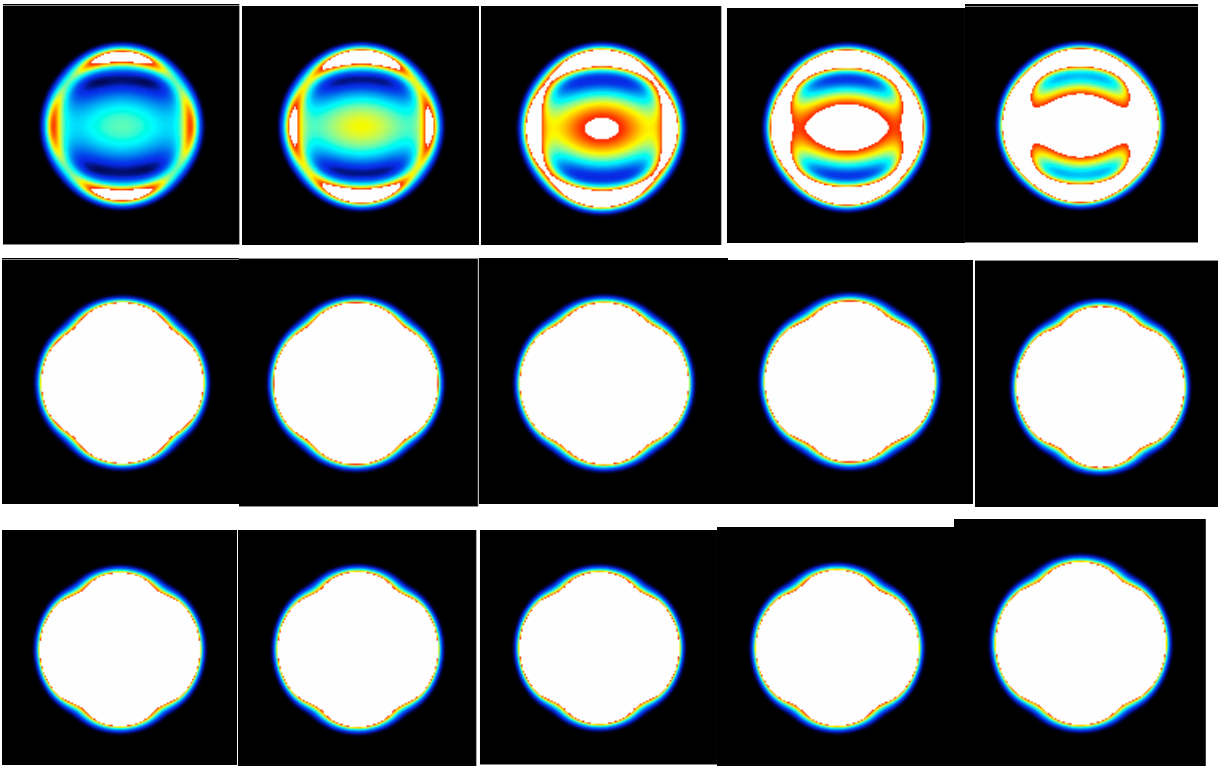




We now present the calculated results for the off resonance excitation of rubidium and as far as we can see, we observe that they are in complete agreement . Later in the populations analysis we will discover the reason .

Fig 8 : calculated P156





We monitored the electron distribution with velocity map imaging applying phase steps and polarization step. The experimental and calculated results for most of the cases are almost identical. We will try to investigate the populations at  $m = -1$  and  $m = 1$ , individual magnetic sub-levels for resonance excitation and off-resonance excitation in order to understand how the excitation efficiencies in those magnetic sub-levels depend from the polarization of the excitation pulse.

In the next figure a schematic lay-out of all the experiment set-up is demonstrated and results from the resonance excitation are discussed.

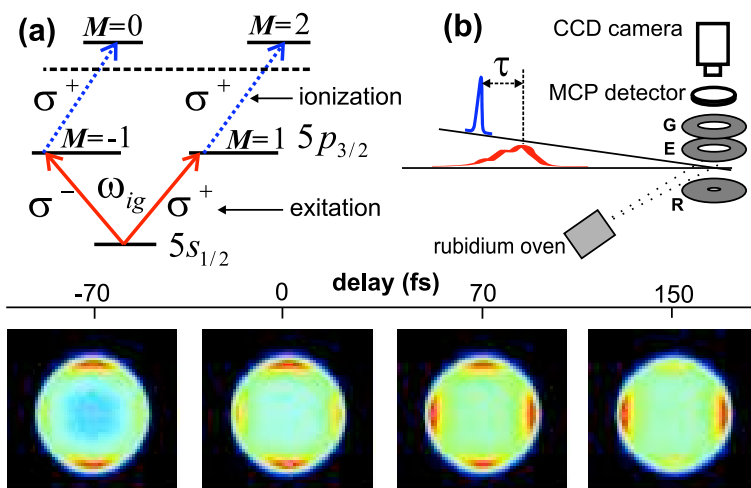


fig 9 : a) the excitation and the probe level scheme b) schematic lay out of the experiment . The angular momentum in the 5p state is probed via an ultra-fast photoionization, using velocity map imaging R, E and G are the repeller , extractor and ground plates respectively. The images show photoelectron angular distributions as a function of time during excitation with the polarization shaped pulse

The laser propagates in vertical direction in the image plane. The images are symmetrized in the plane and normalized to maximum intensity. Red color corresponds to larger intensity. The image at -70 fs shows the photoelectron angular distribution in the case when mostly the  $m = -1$  sub-level is populated. The image at 150 fs represents the case when both sub-levels are equally populated . Non equal intensities for the  $m = -1$  level ( vertical direction ) and the  $m = 1$  ( horizontal direction ) are due to the difference in ionization strength. As can be seen from the images, populations in different Zeeman states provide the distribution with different symmetry. Also , the images show that the angular momentum changes on a 100 fs time-scale during the excitation. Later in this thesis we will explain the procedure of quantifying the  $m = -1$  and  $m = 1$  sub-level populations from the photoelectron angular distributions.

The experimental results during the resonant excitation and the numerical calculations, obtained by time dependent calculation of the Schrodinger equation in the perturbative limit are shown in fig 10.

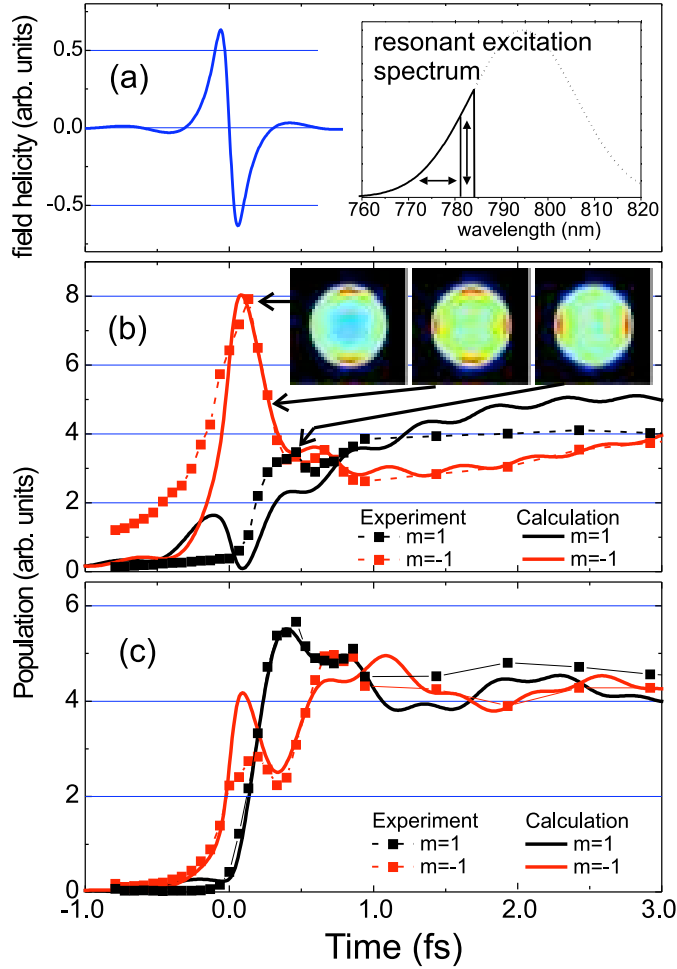


fig 10 : a) pulse field helicity  $\vec{h} = i[\vec{e} \times \vec{e}]$ . The inset shows the excitation spectrum. b) calculated and experimental populations of the  $m = -1$  and  $m = 1$  sub-levels as a function of time. Polarization step is applied at  $\lambda_{ig} + 0.25$  nm c) polarization step applied at  $\lambda_{ig} + 1.25$  nm .

The polarization step was positioned at  $\lambda_{ig} + 0.25$  nm (corresponding to - 0.51 eV ) (fig 10) . In the beginning of the excitation pulse , pure angular momentum is observed in the excited state. After a few hundreds of femtoseconds angular momentum is reserved. Asymptotically the population difference between two Zeeman levels disappears . The images of the photoelectron angular distribution also clearly show change of the angular momentum.

An intriguing result is that the resonant angular momentum dynamics does not correlate with the momentary polarization of the excitation pulse ( fig10 (a)). This non-intuitive effect can be further demonstrated by slightly varying the position of the polarization step relatively to resonance. We applied the polarization step

in the region from  $\lambda_{ig} + 0.25$  nm to  $\lambda_{ig} + 1.25$  nm . While the shape of the excitation pulse remains almost identical to the pulse with spectral polarization step at initial position ( $\lambda_{ig} + 0.25$  nm ) , the angular momentum dynamics changes drastically. In the fig10 (b) the populations of the 5p  $m=1$  and  $m = -1$  sub-levels are presented when the polarization step was applied at  $\lambda_{ig} + 1.25$  nm. The angular momentum changes on a smaller time-scale at larger detuning of the polarization step from resonance. Also , in this case a significant amount of angular momentum of opposite sign is presented in the excited state during the first picosecond.

Our results show that in a resonant one-photon excitation the angular momentum dynamics can not be explained by the dynamics of the polarization of the excitation pulse. In general , in resonant excitation the angular momentum dynamics is determined by the interference between resonant and off-resonant excitation pathways. Hence, for a proper understanding of the mechanisms of the angular momentum transfer, also in one-photon excitation the spectral properties of the pulse should be taken into account.

To demonstrate the role of coherence between the off-resonance spectral components in the dynamics of the angular momentum transfer, we have changed the phases between the spectral components with orthogonal polarization . In the fig 11 the populations of the 5p  $m = 1$  and  $m = -1$  sub-levels are shown when a  $\pi/2$  phase step was applied at the position of the polarization change at  $\lambda_{ig} + 0.25$  nm . This extra step affects the momentary helicity of the pulse. Indeed , a change of the phases in the spectrum clearly affects the angular momentum dynamics. In comparison with the results in the fig 11 the angular momentum changes on a smaller time -scale with almost complete sign inversion during the first 500 fs. Also in this case the angular momentum dynamics does not correlate with the helicity of the excitation pulse (fig 11 (a)).

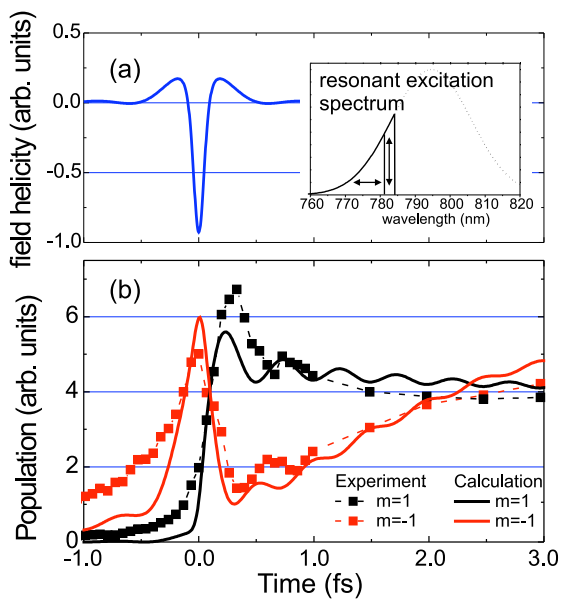


fig 11 : a) pulse field helicity  $\vec{h} = i[\vec{e} \times \vec{e}']$ . The inset shows the excitation spectrum. b) experimental and calculated populations of the  $m=1$  and  $m=-1$  levels as a function of time. Polarization step is positioned at  $\lambda_{ig} + 0.25$  nm and  $\pi/2$  phase step is applied.

We have also performed experiments on control of the angular momentum in a one-photon transition in an off-resonant excitation when a  $\pi/2$  phase step is applied. The excitation spectrum from 780.7 nm to 784 nm was used. The polarization step was positioned at 782.5 nm. The experiment and calculated populations of the 5p  $m=1$  and  $m=-1$  sub-levels are shown in the fig 12.

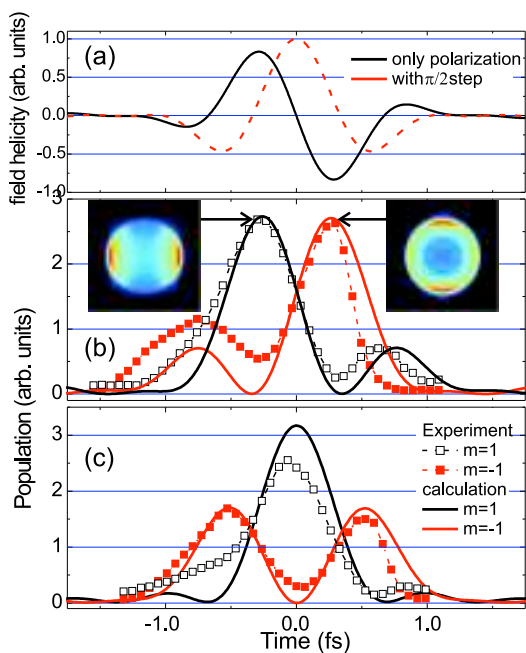


Fig 12: Off resonance excitation . Spectrum part between 780.7 nm and 784 nm is used with polarization at 782.5 nm a) pulse field helicity  $\vec{h} = i[\vec{e} \times \vec{e}]$  . b) experimental and calculated populations of the  $m= 1$  and  $m =-1$  levels as a function of time c)  $P_i / 2$  phase step is applied at position of polarization change.

In an off- resonant excitation the excited state population is only created during the action of the laser pulse. The angular momentum has two major and two minor maxima of opposite sign. The images show reversal of the angular momentum . When the  $\pi/2$  phase step was applied at position of polarization change ( fig 5 (c)), the angular momentum has two maxima of one sign and one larger maximum of opposite sign. During the off-resonant excitation angular momentum dynamics is ideally described by the momentary polarization of the electric field in the pulse. The results clearly show that the angular momentum follows the field helicity of the excitation pulse (fig 12 (a)).

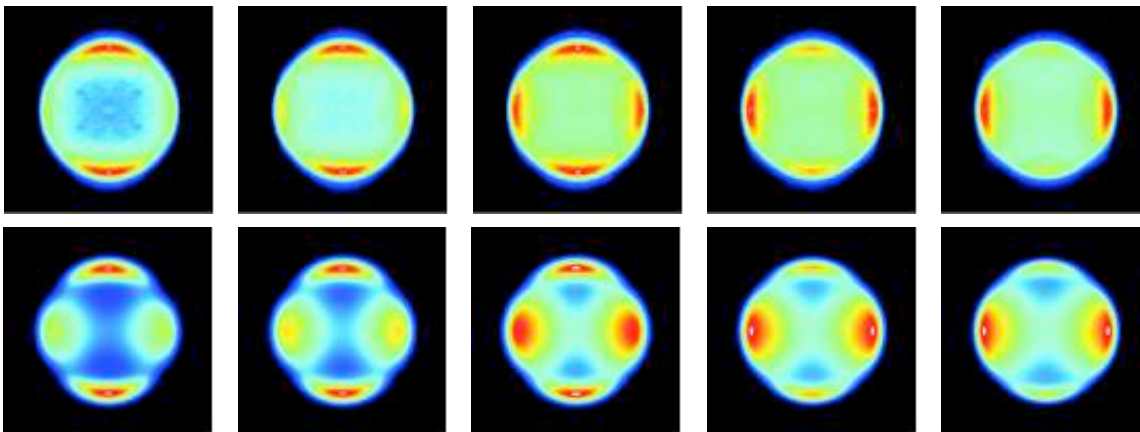


fig 13 : Experimental (top) and calculated (bottom) images of the photo-electron angular distribution. Time step between each image is 67 fs.

### **4.3 Image analysis**

As mentioned before the main purpose of the experiment was to monitor the wave-function induced by the excitation in the 5p state of rubidium.

While it seems plausible that after a sufficiently long time  $t$  the sequence of unsharp position measurements provides enough data to estimate the  $|\Psi_t(q)|^2$ , it may come as a surprise that position measurements enable a faithful monitoring of the full wave-function  $\Psi_t(q)$  as well .

The reason for this is that by measuring the position  $q$  at times  $t = \tau, 2\tau$  on a system with evolving Schrodinger wave-function  $\Psi_t$ , is equivalent to consecutive measurements of the Heisenberg observables  $\hat{q} = \exp(it\hat{H})\hat{q}\exp(it\hat{H})$  on a system with static wave-function  $\Psi_0$  .

The set of Heisenberg coordinates  $\left\{ \hat{q}_t \right\}$  will exhaust a sufficiently large space of incompatible observable so that their measurements will lead to a faithful determination of  $\Psi_0$  . In this way to our faithful determination of  $\Psi_t$ , for long enough times  $t$  .

Concluding monitoring the wave-function means a real time estimation of it .

Returning to rubidium which has three individual magnetic sub-levels  $m = 0, -1, 1$ , we tried to perform coherent control in the first excited state checking excitation efficiencies in those three levels .

The analysis of the angular momentum dynamics in the  $5P_{3/2}$  state was done assuming only orbital angular momentum  $L$ , as well as taking into account the electron spin . In view of the ultra-fast character of the experiment with shaped pulses of a length up to 10 picoseconds, nuclear spin effects can safely be ignored . Here the analysis is presented in the frame of orbital momentum . The excitation and the probe level scheme are shown in Fig 1 . The choice of using

the propagation direction as quantization axis , implies that only the  $m=1$  and  $m=-1$  states are populated. The probe ionization laser is circularly polarized , hence providing only  $\Delta m=+1$  transitions in the ionization step . The angular part of the electronic wave-function in the continuum is presented as coherent superposition of angular momentum states

$$\psi(\theta, \varphi) = \sum_{m,l} \mu_{m,m+1}^l a_m Y_{m+1}^l(\theta, \varphi) e^{-i\xi} \quad (1)$$

where  $m=1$  and  $m=-1$  are the possible Zeeman levels in the intermediate  $5p_{3/2}$  level. The coefficients  $a_m$  are the transition probability amplitudes to the excited  $m$ -states in the  $5p_{3/2}$  state. In the continuum,  $l=0,2$  are the final possible orbital angular momentum state  $\mu_{m,m+1}^l$  is  $m$ -dependent transition dipole moment matrix element between excited state and final state orbital momentum  $l, \xi_l$  is the asymptotic phase of the continuum wave-function , as defined in [17] . The angular distribution measured in the experiment would be  $Y(\theta, \varphi) Y^*(\theta, \varphi)$ .

The goal of the experiment was to determine the populations of  $m = 1$  and  $m = -1$  states as a function of time during excitation . The populations were determined by fitting the experimental images of photoelectron angular distributions with the model , as described in Eq (1). The fitting parameters were absolute the absolute values of  $a_m$  and the relative phase between  $a_{+1}$  and  $a_{-1}$  . In the fitting procedure the intensities in the images were stored line by line in one dimensional vector arrays and the inner product between the experimental and calculated vectors was maximized using Evolutionary Algorithm (ES) [16]. In our fitting procedure, the CMA-ES algorithm developed by Hansen and Ostermeier was used[16]. In the model (see Eq(1)) parameters characterizing outgoing channels with s and d character of the wave-function were taken from [17]. The ratio of the strength between s and d channels was taken from experiment as 0.38. The value of the asymptotic phase difference  $\xi_l$  between s and d channels was 1.7 rad.

## **4.4 Conclusions**

The main purpose of this experiment was to investigate and control ultra-fast dynamics of the angular momentum in an ideal two-level system using as a model atomic rubidium. We wanted to monitor the wave-function of the excited state in a one-photon transition both in resonance and off-resonance. Also employing polarization pulse shaping we wanted to demonstrate an effective control of the femtosecond dynamics of the angular momentum transfer in the excited state.

As a conclusion we have shown that in a one-photon transition the spectral properties of the excitation pulse play a crucial role in the ultra-fast dynamics of the angular momentum transfer. In resonant excitation the angular momentum dynamics in the excited state does not correlate with the helicity of the excitation pulse. In case of an off-resonant excitation the angular momentum follows momentary polarization of the excitation pulse and can be predicted from the time behavior of the polarization.

In conclusion we have demonstrated ultra-fast coherent control of the angular momentum transfer in Rubidium during a one photon excitation. In resonant excitation the angular momentum dynamics can not be explained by polarization dynamics of the excitation pulse and spectral properties of the excitation pulse should be taken into account. in the case of the off-resonant excitation the angular momentum follows momentary polarization of the excitation pulse and can be predicted from the time behavior of polarization. our results give a new insight into ultra-fast control of optical orientation and may provide a new approach to the ultra-fast control of spin orientation.

## References

1. D. Meshulach and Y. Silberberg, *Nature (London)* 396, 239 (1998)
2. Z. Chen et al., *Chem. Phys. Lett.* 198, 498 (1992)
3. J. Stohr and H. C. Siegmann, *Magnetism: From Fundamentals to Nanoscale Dynamics* (Springer, Berlin, 2006)
4. E. Beaurepaire et al., *Phys. Rev. Lett.* 76, 4250 (1996)
5. C. D. Stanciu et al., *Phys. Rev. Lett.* 99, 217204 (2007)
6. G. P. Zhang and W. Hubner, *Phys. Rev. Lett.* 85, 3025
7. J.-Y. Bigot et al., *Nature Phys.* 5, 515 (2009)
8. A. K. Zvezdin and V. A. Kotov, *Modern Magneto-optics and Magneto-optical Materials* (IOP, Bristol, 1997)
9. A. V. Kimel, A. Kirilyuk, and Th. Rasing, *Laser Photon Rev.* 1, 275 (2007)
10. A. V. Kimel et al., *Nature (London)* 435, 655 (2005)
11. N. Dudovich, D. Oron, and Y. Silberberg, *Phys. Rev. Lett.* 92, 103003 (2004)
12. D. A. Malik, A. V. Kimel, A. Kirilyuk, Th. Rasing, and W. J. van der Zande\* *Phys. Rev. Lett.* 104, 133001
13. Zhenghua Wu et al 1994 *J. Phys. B: At. Mol. Opt. Phys.* 27 L457
14. A. Präkelt, M. Wollenhaupt, A. Assion, et. al., *Rev. Sci. Instrum.* 74, 4950 (2003).
15. *Rev. Sci. Instrum.* 68 (9), September 1997
16. N. Hansen, and A. Ostermeier, *Evolutionary Computation*, 9, N°2, 159 (2001).
17. Zheng-Min Wang and D. S. Elliott, *Phys. Rev. A*, 62, 053404 (2000).

